49th AIAA Aerospace Sciences Meeting including the New Horizons Forum and Aerospace Exposition
4 - 7 January 2011, Orlando, Florida
AIAA 2011-367

High-Order Solution-Adaptive Central Essentially Non-Oscillatory (CENO) Method for Viscous Flows

L. Ivan*
Applied Mathematics Department, University of Waterloo
200 University Ave. W., Waterloo, Ontario, N2L 3G1, Canada

C.P.T. Groth†
University of Toronto Institute for Aerospace Studies
4925 Dufferin Street, Toronto, Ontario, M3H 5T6, Canada

A high-order central essentially non-oscillatory (CENO) finite-volume scheme in combination with a block-based adaptive mesh refinement (AMR) algorithm is proposed for solution of the Navier-Stokes equations on body-fitted multi-block mesh. The spatial discretization of the inviscid (hyperbolic) term is based on a hybrid solution reconstruction procedure that combines an unlimited high-order k-exact least-squares reconstruction following from a fixed central stencil with a monotonicity preserving limited linear reconstruction algorithm. The unlimited k-exact reconstruction is used for cells in which the solution is fully resolved and the limited lower-order counterpart is applied to computational cells with under-resolved/discontinuous solution content. Switching in the hybrid procedure is determined by a solution smoothness indicator. The hybrid approach avoids the complexity associated with other ENO schemes that require reconstruction on multiple stencils and therefore, would seem to provide high-order accuracy at lower computational cost and to be very well suited for extension to unstructured meshes. The high-order viscous (elliptic) fluxes are computed based on a k-order accurate gradient derived from the same unlimited high-order reconstructions. A somewhat novel h-refinement criterion based on the solution smoothness indicator is used to direct the steady and unsteady mesh adaptation. The proposed numerical procedure is thoroughly analyzed for advection-diffusion problems characterized by a full range of Péclet numbers, and its predictive capabilities are demonstrated for several laminar flows. The ability of the scheme to accurately represent solutions with smooth extrema and yet robustly handle under-resolved and/or non-smooth solution content is shown. Moreover, the ability to perform mesh refinement in regions of smooth but under-resolved and/or non-smooth solution content to achieve the desired resolution is also demonstrated.

I. Introduction and Motivation

In spite of the rapid advances in high performance computing, there are a number of physically complex flows for which the computational costs of numerical solutions methods can make the simulations of such flows prohibitive and/or non-routine. Such flows would include but are certainly not limited to compressible turbulent and turbulent reactive flows through aerospace propulsion systems. It is felt that effective numerical solution methods for such complex flows may require both high-order discretizations and adaptive mesh refinement (AMR). Moin and Krishnan[1] point out that even ENO schemes as high as sixth-order can be too dissipative for the prediction of shock/turbulence interactions without refinement of the mesh in the vicinity of the shock wave and, in other work, Jameson[2] has shown that high-order methods can be considerably more efficient than low-order AMR schemes for flows containing structures such as vortices, eddies and/or

*Postdoctoral Fellow, Email: livan@math.uwaterloo.ca, Student Member AIAA.
†Professor, Email: groth@utias.utoronto.ca, Senior Member AIAA.

turbulence and concluded that high-order schemes combined with AMR may provide very effective means of obtaining high solution accuracy.

In the last decades, there have been numerous studies of high-order schemes. For hyperbolic conservation laws and/or compressible flow simulations, the challenge has been to achieve accurate discretizations while coping in a reliable and robust fashion with discontinuities and shocks. The essentially non-oscillatory (ENO) finite-volume schemes first proposed by Harten *et al.*[3] provide robust frameworks for high-order finite-volume discretizations of hyperbolic systems. The original ENO scheme of Harten *et al.* is based on an adaptive-stencil strategy, in which the stencil leading to the "smoothest" reconstruction is selected and thereby stencils containing discontinuities are avoided. Although original developed for structured regular mesh, Abgrall[4] and Sonar[5] have since extended the ENO concept for application to unstructured grids. In addition, so-called weighted ENO (WENO) schemes have been developed for both structured and unstructured meshes.[6–8] Nevertheless, the difficulty with these high-order approaches has been the extension of the method to multi-dimensional problems and large systems of couple partial differential equations (PDEs). The computational challenges are primarily related to the stencil selection, particularly in the case of unstructured grids,[4,5,9,10] and the poor conditioning of the linear systems that define the reconstructions for these stencils.[9,10] The requirement of using a different stencil for each flow variable is also somewhat problematic, particularly for systems with many dependent solution variables. Other perceived challenges associated with ENO and WENO high-order finite-volume schemes are the relatively large non-compact stencils which can give rise to difficulties with the application of boundary data and efficicient parallel implementation of the algorithm. Although successful implementations of this class of finite-volume scheme have been developed, in general the computational costs and complexity of the schemes have limited their widespread application. Nevertheless, combinations of high-order ENO and WENO schemes with AMR for both structured and unstructured meshes have been developed and applied to engineering problems, such as the prediction of high-speed flows as described in the recent work by Wolf and Azevedo.[11]

Other researchers have considered more flexible high-order finite-volume schemes, which may be more easily extended to multi-dimensional problems and to unstructured meshes. For example, Barth and Fredrickson[12,13] developed a high-order finite-volume approach for unstructured mesh based on k-exact least-squares reconstruction. Following on their work, Ollivier-Gooch[14,15] has more recently proposed a data-dependent weighted least-squares reconstruction procedure (DD-ENO), that uses a fixed stencil and seeks to enforce monotonicity of the scheme by introducing data-dependent weights for each point in the stencil. To circumvent some deficiencies in the DD-ENO procedure, Ollivier-Gooch *et al.* reconsidered the use of non-linear limiters for controlling oscillations and defined a high-order limiting strategy in combination with a k-exact reconstruction procedure.[16,17] Capdeville recently revisited the DD-ENO concept and formulated a compact Hermite least-square monotone (HLSM) reconstruction scheme in one-dimension.[18] Additionally, Colella *et al.*[19] have developed a high-order finite-volume method in mapped coordinates for discretization of linear elliptic and hyperbolic PDEs. Their approach has been already extended to nonlinear systems of hyperbolic conservation laws on locally-refined grids by McCorquodale and Colella.[20] To suppress undesirable solution oscillations, the latter authors applied a fairly elaborate combination of slope limiters, slope flattening, and artificial viscosity. Moreover, their proposed multidimensional limiting strategy employs a modified version of the one-dimensional limiter formulated by Colella and Sekora[21] for preserving accuracy at smooth extrema.

High-order finite-element schemes have also been considered for problems involving discontinuities. In particular, the class of schemes now generally referred to as discontinuous Galerkin (DG) schemes have gained in popularity. Cockburn *et al.*[22–24] were the first to formulate a family of high-order total variation bounded schemes for nonlinear systems of conservation laws referred to as Runge-Kutta discontinuous Galerkin (RKDG) methods. By combining elements from the finite-element and finite-volume methods, Cockburn *et al.* have obtained a family of numerical schemes that improve the data locality and yet allow for discontinuous solution spaces. Hence, a flexible high-order spatial discretization with a greatly reduced stencil size can be formulated. The reduced stencil is beneficial for both boundary-condition implementation and algorithm parallelization. To ensure non-oscillatory properties of the predicted solutions near discontinuities and/or large gradients, DG methods have been considered in combination with different limiting strategies, such as TVB-[24] and WENO-type[25] limiters. Additionally, Barter and Darmofal[26] formulated a DG scheme with a PDE-based artificial viscosity model to avoid spurious numerical oscillations in the proximity of shocks. Xu *et al.*[27] have also recently applied a hierarchical reconstruction (HR) strategy to DG methods in combination with a WENO-type linear reconstruction in each hierarchical level. Despite the interest generated by DG methods over the last decade, high-order DG schemes do suffer from a more

restrictive time-step stability limit that is exacerbated as the solution order is increased[28] and from a relatively high computational cost per cell associated with the solution of the additional unknowns within each cell. The former can be particularly problematic for explicit time-marching schemes. Partly in response to the latter, it is noted that Dumbser *et al.*[29] have recently formulated a unified framework for finite-volume and discontinuous Galerkin methods on unstructured mesh which introduces a new family of reconstructed DG schemes denoted as $P_N P_M$ methods.

In other work, Wang *et al.*[30,31] and Liu *et al.*[32] have proposed variants of the DG formulation, referred to as spectral volume (SV) and spectral difference (SD) methods, for obtaining high-order solutions to hyperbolic conservation equations. In fact, DG, SV and SD methods share many similarities, the main difference consisting in how the degrees of freedom of each scheme are chosen and updated. A new perspective regarding the DG, SV and SD methods has been introduced by Huynh,[33] who was able to recover all these methods in one-space dimension as particular cases of a general formulation based on a flux reconstruction (FR) approach to high-order schemes for hyperbolic laws. For dealing with undesirable solution oscillations, the SV and SD methods have been usually considered in combination with total variation diminishing (TVD) limiting strategies. However, Yang and Wang[34,35] have recently combined a SD scheme for arbitrary unstructured grids with a compact high-order hierarchical moment limiter. More recently, Wang and Gao[36,37] have generalized Huynh's flux reconstruction approach to mixed grids and formulated a unifying lifting collocation penalty (LCP) method for Euler equations and applied it to smooth flows. An advantage of their unified formulation is that the relative cost of LCP method with respect to a DG scheme was inferred easily by simply comparing the main operations required for the two algorithms. In addition, the newly proposed LCP formulation is shown to be more efficient in both memory and CPU time than DG methods. Alternative high-order schemes, such as residual distribution schemes[38–41] and finite-difference algorithms,[42] have also been developed and are currently being pursued for application on either unstructured and/or multi-block structured meshes.

High-order schemes for PDEs governing diffusion processes and/or having a more elliptic nature have also been considered. In these cases, it is desirable that the discretization of the elliptic operator remain accurate while satisfying a maximum principle, even on stretched/distorted meshes.[43,44] Standard lower-order spatial discretizations may not even always have these characteristics. Sun *et al.*[45] and May and Jameson[46,47] have considered the applications of the SV and SD methods, respectively, to viscous flows. The latter have also applied their scheme in combination with AMR to the Navier-Stokes system of equations. More recently, Gao and Wang[48] and Haga *et al.*[49] have applied the LCP formulation to Navier-Stokes equations on two- and three-dimensional mixed grids, respectively. Barad and Colella have proposed a fourth-order-accurate AMR scheme for Poisson's equation[50] and Ollivier-Gooch and van Altena[51] describe a general high-order framework for the solution of the advection-diffusion equation on unstructured mesh. In other work on diffusion problems on unstructured grids, van Leer *et al.*[52,53] proposed a recovery-based DG method that eliminates the introduction of *ad hoc* penalty or coupling terms found in traditional DG methods. More recently, Oliver and Darmofal[54] applied the DG with a PDE-based artificial viscosity model to aerodynamic flows governed by RANS equations. Finally, De Rango and Zingg[55] have considered the application of high-order finite-difference methods to the prediction of turbulent aerodynamic flows.

In spite of the advances in high-order accurate methods, there is still no consensus for a robust, efficient, and high-order accurate scheme that fully deals with all of the aforementioned issues and is applicable to more arbitrary meshes and complex boundary-condition problems. In the current work, the high-order central ENO (CENO) cell-centred finite-volume scheme proposed by Ivan and Groth[56] for inviscid flows is extended to the solution of the Navier-Stokes equations governing two-dimensional, compressible, viscous flows on body-fitted multi-block mesh. The CENO discretization of the inviscid (hyperbolic) flux is based on a hybrid solution reconstruction procedure that combines the unlimited high-order k-exact least-squares reconstruction technique of Barth[12] based on a fixed central stencil with a monotonicity preserving limited piecewise linear least-squares reconstruction algorithm.[12] Switching in the hybrid procedure is determined by a solution smoothness indicator that specifies whether or not the solution is resolved on the computational mesh. The limited reconstruction procedure is applied to computational cells with discontinuous and under-resolved solution content and the unlimited k-exact reconstruction scheme is used for cells in which the solution is fully resolved. In order to guarantee a global k-order accurate numerical scheme on arbitrary meshes, the proposed discretization of the viscous (elliptic) flux is based on a k-order accurate average gradient derived from a $k+1$-order accurate reconstruction (one order higher than what would be normally required to obtain a k-order accurate inviscid flux). This same solution reconstruction is used in comput-

ing both the inviscid and elliptic fluxes. The high-order finite-volume CENO scheme is combined with a flexible block-based hierarchical data structure to facilitate parallel implementation via domain decomposition and automatic solution-directed mesh adaptation on body-fitted multi-block quadrilateral mesh.[57] An h-refinement criterion based on the solution smoothness indicator to control the refinement of the multi-block AMR mesh.

In what follows, the proposed high-order CENO finite-volume method, block-based AMR procedure, and high-order treatment of boundary data are all described. The properties of the proposed CENO scheme are investigated by comparing numerical solutions to analytical solutions for a range of problems pertaining to the simple advection-diffusion model equation. The accuracy of the hyperbolic flux discretization for systems of equations is demonstrated for solutions of the Euler equations governing inviscid flows. Furthermore, the predictive capabilities of the proposed approach for laminar viscous flows governed by the full Navier-Stokes equations are demonstrated by comparing numerical predictions to numerical and experimental results reported in the literature for flow past a circular cylinder. Finally, results obtained with the CENO scheme in conjunction with AMR are also described to illustrate the capabilities of the proposed combined approach.

II. Conservation Equations

The proposed high-order finite-volume method is applied herein to solutions of both the scalar advection-diffusion and Navier-Stokes equations governing laminar compressible flows. The advection-diffusion equation is a very convenient mathematical model for the development of numerical solution algorithms for it contains many of the features of more complicated PDEs, yet it retains a simplicity that readily permits direct analysis. The particular form considered herein is given by

$$\underbrace{\frac{\partial u}{\partial t}}_{\text{Transient term}} + \underbrace{\vec{\nabla}\cdot(\vec{V}(\vec{r},u)\,u)}_{\text{Advective term}} = \underbrace{\vec{\nabla}\cdot(\kappa(\vec{r},u)\,\vec{\nabla}u)}_{\text{Diffusive term}} + \underbrace{\phi(\vec{r},u)}_{\text{Source term}} \quad , \tag{1}$$

where t is the time, u is the solution (a scalar quantity), $\vec{V}$ is the advection velocity vector, κ is the diffusion coefficient, and ϕ is a non-linear source term. In the most general case, $\vec{V}$ and κ are functions of the position vector, $\vec{r}$, as well as the solution, u. Based on the relative magnitudes of the advective and diffusive fluxes, the solutions of this equation can range from those having a more hyperbolic nature and governed by wave propagation phenomena to those having a more elliptic nature and governed by diffusive processes. Therefore, it is very desirable that numerical schemes for the solution of this equation do not introduce excessive artificial dissipation, large dispersive error, and spurious oscillations arising from the discretization of the hyperbolic term, and provide accurate discretizations of the elliptic term while satisfying a maximum principle.[58,59]

The Navier-Stokes equations governing viscous compressible gaseous flows can be written generally in the following form:

$$\frac{\partial \mathbf{U}}{\partial t} + \vec{\nabla}\cdot\vec{\mathbf{F}} = \frac{\partial \mathbf{U}}{\partial t} + \vec{\nabla}\cdot\vec{\mathbf{F}}_{\mathrm{H}}\left(\mathbf{U}\right) + \vec{\nabla}\cdot\vec{\mathbf{F}}_{\mathrm{E}}\left(\mathbf{U},\vec{\nabla}\mathbf{U}\right) = 0\,, \tag{2}$$

where $\mathbf{U}$ is the vector of conserved solution variables and $\vec{\mathbf{F}}$ is the solution flux dyad. The solution flux, $\vec{\mathbf{F}}$, is the sum of a hyperbolic (inviscid) term, $\vec{\mathbf{F}}_{\mathrm{H}}$, which depends on the solution vector and accounts for transport by wave phenomena and an elliptic (viscous) term, $\vec{\mathbf{F}}_{\mathrm{E}}$, associated with diffusion processes and therefore, dependent on both the solution vector and its gradient. For two-dimensional planar flows, the solution vector, $\mathbf{U}$, is given by

$$\mathbf{U} = \left[\ \rho,\ \ \rho v_x,\ \ \rho v_y,\ \ \rho e\ \right]^T\,, \tag{3}$$

where ρ is the gas density, v_x and v_y are the velocity components in the x- and y-coordinate directions, $e = p/(\rho(\gamma-1)) + (v_x^2+v_y^2)/2$ is the specific total energy, $p = \rho RT$ is the pressure, T is the gas temperature, R is the gas constant, γ is the specific heat ratio. The components of the hyperbolic flux dyad, $\vec{\mathbf{F}}_{\mathrm{H}}(\mathbf{F},\mathbf{G})$, and elliptic flux dyad, $\vec{\mathbf{F}}_{\mathrm{E}}(\mathbf{F}_{\mathrm{v}},\mathbf{G}_{\mathrm{v}})$, in this case are then given by

$$\mathbf{F} = \ \ [\rho v_x, \rho v_x^2 + p, \rho v_x v_y, v_x(\rho e + p)]^{\mathrm{T}}\,, \quad \mathbf{G} = \ \ [\rho v_y,\, \rho v_x v_y\,, \rho v_y^2 + p, v_y(\rho e + p)]^{\mathrm{T}}\,, \tag{4}$$

and

$$\mathbf{F}_{\mathrm{v}} = -[0, \tau_{\mathrm{xx}}, \tau_{\mathrm{yx}}, v_x\tau_{\mathrm{xx}} + v_y\tau_{\mathrm{xy}} - q_{\mathrm{x}}]^{\mathrm{T}}\,, \quad \mathbf{G}_{\mathrm{v}} = -[0,\, \tau_{\mathrm{xy}}, \tau_{\mathrm{yy}}, v_x\tau_{\mathrm{yx}} + v_y\tau_{\mathrm{yy}} - q_{\mathrm{y}}]^{\mathrm{T}}\,. \tag{5}$$

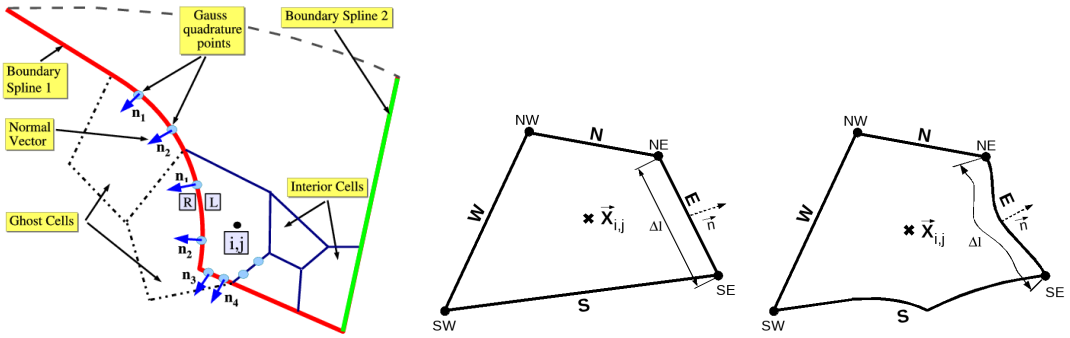

(a) Geometric elements near curved boundaries (b) A straight-edge quadrilateral (c) A curved-edge quadrilateral

Figure 1. (a) Schematic representation of geometric elements at the boundaries of a body-fitted quadrilateral mesh; and (b) the straight-edge and (c) the curved-edge convex quadrilateral elements considered in this work. Cardinal directions (i.e., N, S, E, W) relative to the element centroid, $\vec{X}_{i,j}$, are used to identify each face and node of the quadrilateral. The figure also shows the unit outward vector normal, $\vec{n}$, at a given location and the length of a face, $\Delta\ell$.

The components τ_{xx}, τ_{yy} and τ_{xy} of the fluid stress tensor, $\vec{\vec{\tau}}$, are given by $\vec{\vec{\tau}} = 2\mu(\vec{\vec{S}} - \frac{1}{3}\vec{\vec{I}}\,\vec{\nabla}\cdot\vec{V})$, where μ is the dynamic viscosity and $\vec{\vec{S}} = \frac{1}{2}\left[\vec{\nabla}\vec{V} + (\vec{\nabla}\vec{V})^{\mathrm{T}}\right]$ is the strain rate tensor. The heat flux vector, $\vec{q}(q_x, q_y)$, follows from Fourier's law of heat conduction and is given by $\vec{q} = -\kappa\vec{\nabla}T$, where κ is the thermal conductivity. For a calorically perfect polytropic gas, the ratio of specific heats, γ, is a constant and the specific heats are given by $C_v = R/(\gamma - 1)$ and $C_p = \gamma R/(\gamma - 1)$. All of the results included herein correspond to diatomic gases for which $\gamma = 1.4$.

III. High-Order CENO Finite-Volume Scheme

In the present work, a high-order central essentially non-oscillatory (CENO) cell-centred finite-volume scheme is proposed for solving the mixed type system of conservation laws given by Eq. (2) on body-fitted multi-block quadrilateral mesh in conjunction with a block-based adaptive mesh refinement technique. Use of this particular grid structure and AMR strategy has been shown to allow highly efficient and scalable parallel implementations of finite-volume methods.[57]

Each single-block mesh constituent of the body-fitted multi-block grid has associated a structured quadrilateral grid and the boundary geometry defined by four body-fitted curved boundaries which are provided as piecewise Lagrange polynomial splines of an order consistent with that of the finite-volume numerical scheme. Note that inter-block boundaries are always represented by straight segments and only the physical block boundaries need to be represented by body-fitted splines. A schematic representation of geometric elements encountered near the curved geometric boundaries is depicted in Fig. 1(a). The convex quadrilateral element types considered in this work are shown in Fig. 1(b) and (c). A distinctive feature of the current algorithm as compared to previous lower-order implementations on similar meshes[57,60–62] is the high-order treatment of curved physical boundaries, obtained through the introduction of quadrilaterals having curved edges as shown in Fig. 1(c), in which the connector between any two adjacent boundary mesh nodes is a piecewise-smooth curved line. Note that straight-edge quadrilaterals are always used for interior cells whereas curved-edged quadrilaterals may be required for representing the boundaries of body-fitted mesh with high-order accuracy.

III.A. Semi-Discrete Form

The finite-volume method used herein starts from the integral form of Eq. (2) for a two-dimensional polygonal control volume, (i, j), and makes use of the divergence theorem to arrive at the following semi-discrete form:

$$\frac{d\overline{\mathbf{U}}_{i,j}}{dt} = -\frac{1}{A_{i,j}}\sum_{l=1}^{N_f}\sum_{m=1}^{N_G}\left(\omega\vec{\mathbf{F}}\cdot\vec{n}\,\Delta\ell\right)_{i,j,l,m} = \mathbf{R}_{i,j}(\overline{\mathbf{U}})\,, \tag{6}$$

where

$$\overline{\mathbf{U}}_{i,j} = \frac{1}{A_{i,j}} \iint_{\mathcal{A}_{i,j}} \mathbf{U} \; da \tag{7}$$

is the average value of the conserved solution vector for cell (i,j), the vector $\mathbf{R}_{i,j}$ is the so-called residual vector, and $A_{i,j}$ is the area of the cell. A N_G-point Gaussian quadrature integration procedure is used evaluate the solution flux along each of the N_f faces of the cell where ω is the quadrature weighting coefficient and $\Delta\ell$ and $\vec{n}$ are the length of the cell face and unit vector normal to the cell face or edge, respectively.

Equation (6) describes the time evolution of the solution, $\overline{\mathbf{U}}$. The proposed finite-volume scheme involves three major steps when integrating this equation forward in time: 1) **reconstruction** in which an approximation to $\mathbf{U}(\vec{X})$ is obtained within each computational cell; 2) **residual evaluation** which the residual vector, $\mathbf{R}$, is evaluated in each cell based on the reconstructed solution; and 3) **time integration**, in which a time-marching scheme is used to advance the solution to the next time level based on the solution residual. The remainder of this section presents the details each of these steps with an emphasis on the methodology used for obtaining high-order solutions.

III.B. Explicit Temporal Discretization Methods

As the efficiency of the temporal descritization was not the focus here, the time integration of Eq. (6) is carried out using standard explicit time-marching schemes. For steady, time-invariant problems, for which $\mathbf{R}_{i,j}(\overline{\mathbf{U}}) = 0$, explicit optimally-smoothing multi-stage scheme developed by van Leer *et al.*[63,64] were used. For time-accurate calculations, the time marching scheme was matched with the spatial accuracy and either a two- or four-stage standard Runge-Kutta scheme[65–67] was used, depending on the accuracy of the spatial reconstruction.

III.C. Numerical Residual Evaluation

High-order accurate solutions of Eq. (6) are sought here in two space dimensions by applying a high-order spatial discretization to the solution residual vector, $\mathbf{R}_{i,j}$, in conjunction with high-order polynomial solution reconstruction, upwind discretization of the hyperbolic flux and centrally weighting discretization of the elliptic flux. Thus, the high-order CENO numerical procedure requires the computation with high-order accuracy of the integrals making up the spatial residual while ensuring the stability of the numerical scheme.

The high-order accurate numerical computation of the net flux through the boundary of a computational cell (i.e., the flux contour integral) starts with the selection in Eq. (6) of a number of Gauss quadrature points, N_G, dictated by the desired order of solution accuracy at which the numerical flux, $\vec{\mathbf{F}} \cdot \vec{n}$, is evaluated.[13] For high-order accuracy the numerical flux representing the sum of the non-linear hyperbolic and elliptic fluxes, $\vec{\mathbf{F}} \cdot \vec{n} = \vec{\mathbf{F}}_{\mathrm{H}}(\mathbf{U}) \cdot \vec{n} + \vec{\mathbf{F}}_{\mathrm{E}}(\mathbf{U}, \vec{\nabla}\mathbf{U}) \cdot \vec{n}$, needs to be estimated at each quadrature point, m, of a cell face, l, with a flux function that approaches the *true* flux at the rate imposed by the expected order of accuracy in the asymptotic limit of infinitely small mesh size. This requirement translates to a similar set of conditions on the accuracy of the solution state, $\mathbf{U}$, and solution gradient, $\vec{\nabla}\mathbf{U}$, used to calculate both the hyperbolic, $\vec{\mathbf{F}}_{\mathrm{H}}$, and elliptic, $\vec{\mathbf{F}}_{\mathrm{E}}$, fluxes. Other than this, the flux function is required to produce a dissipative and stable scheme.

In this work, the hyperbolic flux at each inter-cellular face is determined using a high-order upwind formulation, originally pioneered by Godunov.[68] Consequently, the procedure for computing the hyperbolic flux at a cell interface is based on the wave structure emerging at an interface with discontinuous solution data, which is equivalent to solving a local Riemann problem with the left and right solution states, $\mathbf{U}_l$ and $\mathbf{U}_r$, as initial data.[69] Thus, the hyperbolic normal flux at each quadrature point is given by $\vec{\mathbf{F}}_{\mathrm{H}} \cdot \vec{n} = \mathcal{F}(\mathbf{U}_l, \mathbf{U}_r, \vec{n})$, where the numerical flux $\mathcal{F}$ is evaluated by solving the Riemann problem in a direction defined by the normal to the face with $\mathbf{U}_l$ and $\mathbf{U}_r$. In the present algorithm, both exact and approximate Riemann solvers can be used to solve the Riemann problem and evaluate the numerical flux. Details of the flux functions considered herein for each of the governing equation sets described in Sect. II are given in Sect. III.E.

The left and right solution states, $\mathbf{U}_l$ and $\mathbf{U}_r$, are determined by performing piecewise k-order polynomial solution reconstruction within each computational cell, which obviously makes the spatial accuracy of the finite-volume scheme very dependent on the order of the solution reconstruction. Since the truncation error for k-order exact reconstruction is $\mathcal{O}(\Delta x^{k+1})$, a $(k+1)$-order accurate spatial discretization can be achieved based on this reconstruction for smooth hyperbolic problems. Consequently, the number of Gauss quadrature points at which the numerical flux is evaluated is chosen on the basis of the order of the solution

reconstruction. To determine the optimum number of quadrature points for a desired accuracy recall that an N-point Gaussian quadrature rule integrates polynomials of degree $2N-1$ exactly, providing a $2N$-order accurate formula.[70] Following this rule, the practise adopted here is to use one quadrature point ($N_G=1$) for second-order schemes (piecewise linear, $k=1$, reconstruction) and two quadrature points ($N_G=2$) for third- and fourth-order schemes (piecewise quadratic, $k=2$, and cubic, $k=3$, reconstruction) to ensure that the order of accuracy of the schemes is preserved. Ample details of the polynomial solution reconstruction considered in this work are provided in Sect. III.D.

In a similar manner to hyperbolic fluxes, numerical elliptic fluxes, $\vec{\mathbf{F}}_{\mathrm{E}} \cdot \vec{n}$, must be evaluated at each quadrature point of each computational cell face. High-order elliptic fluxes can be calculated by using information from the $(k+1)$-order accurate solution approximation obtained in the reconstruction step. Note that a $(k+1)$-order accurate solution reconstruction will usually produce a k-order accurate gradient (i.e., one order less due to differentiation), which should in turn lead to a k-order accurate flux evaluation and finally, a k-order accurate flux integral. It is thus inferred that a $(k+1)$-order accurate spatial discretization scheme for *both* hyperbolic and elliptic terms on arbitrary meshes, implies the use of a k-order exact gradient (i.e., a gradient with $(k+1)$-order truncation error) for the evaluation of elliptic fluxes, which here is derived from a $(k+1)$-order exact reconstruction. Thus, having determined the left and right $(k+1)$-order exact piecewise solution reconstructions, $U_l^{k+1}(\vec{X})$ and $U_r^{k+1}(\vec{X})$, a unique k-order exact solution gradient at the inter-cellular face is obtained as the arithmetic mean of the left and right reconstruction gradients. Note that, the arithmetic mean procedure may provide a $(k+1)$-order exact gradient from two $(k+1)$-order exact reconstructions if error cancellation occurs, a situation which can arise only for odd reconstruction orders and for generally regular meshes.

Finally, to obtain a consistent and accurate scheme for *both* hyperbolic and elliptic operators with $(k+1)$-order exact solution reconstruction and a k-order exact gradient, the optimum number of Gauss integration points for the elliptic flux is used for each cell face. Consequently, consistent 3rd- and 4th-order accurate schemes are formed here for piecewise cubic and quartic reconstructions ($k=3$ and $k=4$) with two quadrature points ($N_G=2$).

III.D. CENO Reconstruction

A high-order central ENO (CENO) method is used herein for performing the piecewise k-order polynomial reconstruction within each of the computational cells. This new ENO variant aims to overcome some of the practical drawbacks of other ENO and WENO schemes for application to multi-dimensional problems with large numbers of unknowns, which are generally associated with the stencil selection algorithm, the large computational cost resulting from carrying out multiple reconstructions on different stencils, that may also be different for each solution variable, and the necessity to employ extra algorithms for dealing with singular stencils[10] and occurrence of negative weights,[71] especially on unstructured meshes. In addition, the original ENO-type reconstructions may lead to negative values of density and pressure due to their design principle (i.e., selection of the "smoothest" stencil) which does not strictly enforce solution monotonicity[4,72] and the WENO weights may require some tuning such that the central stencil, recognized to be the most accurate one, is recovered in the smooth parts of the solution.[73,74] Despite all these drawbacks, both ENO and WENO schemes provide a solid starting point for the search for more effective high-order discretizations.

The proposed CENO variant is not based on either selecting or weighting reconstructions from multiple stencils. Instead, a hybrid solution reconstruction procedure is used that combines the high-order k-exact least-squares reconstruction technique of Barth[12] based on a *fixed central stencil* with a monotonicity preserving limited piecewise linear least-squares reconstruction algorithm.[12] Due to cancellation of truncation errors, use of the central stencil will generally provide the most accurate reconstruction. In case of unstructured mesh, the *central stencil* should be interpreted as a stencil that includes all nearest neighbour cells up to a specified order. In the CENO approach a limited reconstruction procedure is applied to computational cells with under-resolved solution content, thereby avoiding undesirable solution oscillations (wiggles), and the unlimited k-exact reconstruction scheme is used for cells in which the solution is fully resolved. Switching in the hybrid procedure is determined by a solution smoothness indicator that specifies whether or not the solution is resolved on the computational mesh. This hybrid approach avoids the complexity associated with other ENO and WENO schemes that require reconstruction on multiple stencils which in some cases can produce poorly conditioned coefficient matrices. Additionally, the same fixed stencil is used for each variable and the solution of the least-squares problem for the reconstruction can then be made quite efficient. For this reason, the hybrid CENO algorithm would seem very well suited for application to unstructured mesh.

Moreover, mesh adaptation can be directed based on the ability of the CENO scheme to differentiate between resolved and under-resolved or non-smooth solution content.

The CENO reconstruction leads to a finite-volume scheme for hyperbolic conservation equations that is high-order accurate for smooth solutions even near extrema and avoids the appearance of $O(1)$ numerical oscillations in under-resolved regions and for solutions containing strong discontinuities and/or shocks. Note however that in the proposed formulation the formal ENO property of uniform accuracy is lost for non-smooth solutions. Accuracy to any order is possible by simply expanding the support for the cell-centred reconstruction. Note that in earlier work, Harten and Chakravarthy[75] have proposed a technique to obtain an ENO reconstruction on a fixed central stencil by hybridizing the high-order reconstruction with a first-order formulation. The switching in their proposed hybrid central ENO scheme was based on undivided differences and the total variation diminishing (TVD) property[76] and not directly on the smoothness of the reconstructions. More recently, Haselbacher[10] has since explored the use of fixed stencil central reconstruction in the formulation of WENO schemes for unstructured mesh, but Haselbacher's approach is somewhat different to the current approach and schemes of accuracy higher than second order ($k=1$) were not formulated.

The reconstruction operation is a strictly-mathematical procedure in which no physical characteristics of the problem are directly included and depends solely on the average solution states provided as input data. Consequently, it can be equally applied to any of the independent solution variables regardless of their physical meaning and of whether they represent conserved, primitive or characteristic quantities. In our computational framework for multivariate PDEs we prefer to perform the reconstruction with the primitive solution states whereas the solution update is carried out with the conserved variables. To map the average conserved into average primitive states and vice-versa our algorithm applies the same relationships as those used for pointwise mapping. An exact conversion between the two types of average quantities cannot be obtained for non-linear relationships with this approach. Very recently, McCorquodale and Colella[20] have proposed a mapping which provides a fourth-order accurate conversion between the aforementioned solution variables. Although no corrections have been considered herein, it seems that the error introduced by the pointwise-based conversion of the average quantities does not seem to affect the order of accuracy of the high-order scheme, a fact demonstrated in Sect. V.F by numerical experiments with both sets of variables.

In what follows, a summary of the high-order CENO reconstruction described in detail in[77] is provided.

III.D.1. k-Exact Least-Squares Reconstruction

In piecewise k-exact polynomial reconstruction,[12] it is assumed that a solution variable, u, at any location, $\vec{X}$, in computational cell (i,j) has the general form

$$u^k_{i,j}(\vec{X}) = \sum_{\substack{p_1=0 \\ (p_1+p_2\leq k)}}^{k} \sum_{p_2=0}^{k} (x-\bar{x}_{i,j})^{p_1} \, (y-\bar{y}_{i,j})^{p_2} \, D^k_{p_1 p_2} \ , \tag{8}$$

where (x,y) are the Cartesian coordinates of the position vector, $\vec{X}$, at the point of interest, $(\bar{x}_{i,j}, \bar{y}_{i,j})$ are the coordinates of the cell centroid $\vec{X}_{i,j}$, k is the order of the piecewise polynomial interpolant, the summation indices p_1 and p_2 must satisfy the condition that $p_1 + p_2 \leq k$, and $D^k_{p_1 p_2}$ are the coefficients of the k-exact polynomial approximation to be determined. The latter are in general functions of the mean or average value solution, $\bar{u}_{i,j}$, within the cell and its neighbours. For a 2D reconstruction, the number of coefficients, $\mathcal{N}_D$, for a particular order k and one solution variable is given by $\mathcal{N}_D = \frac{(k+1)(k+2)}{2}$. For example, a cubic reconstruction, $k=3$, has $\mathcal{N}_D = 10$ unknown coefficients for each solution variable.

To determine $D^k_{p_1 p_2}$ the following conditions are required to be satisfied by the reconstruction procedure: 1) the reconstruction procedure must reproduce exactly polynomials of degree $N \leq k$; 2) the reconstruction must preserve the mean or average value within the computational cell; 3) the reconstruction must have compact support. The first condition is equivalent to $u^k_{i,j}(\vec{X} - \vec{X}_{i,j}) - u_{\text{exact}}(\vec{X}) = \mathcal{O}(\Delta x^{k+1})$, which is assumed to hold anywhere in the vicinity of cell (i,j). The second condition requires the integral of the piecewise polynomial approximation to recover the cell average data, which gives $\bar{u}_{i,j} = \frac{1}{A_{i,j}} \iint_{\mathcal{A}_{i,j}} u^k_{i,j}(\vec{X}) dx \, dy$. Finally, the third condition involves the number and locality of the neighbouring solution states used in the so-called *reconstruction supporting stencil*. The minimum size of the compact stencil is determined by the number of required unknown coefficients, but in practise, additional neighbours are included in order to make the reconstruction more robust in the presence of stretched meshes and solution gradients not aligned

with the mesh. For body-fitted quadrilateral mesh, the current k-exact reconstruction scheme uses a fixed central stencil which includes 8 neighbour cells for $k=1$ and 24 neighbours for $k=2,3$ and 4.

The evaluation of the coefficients $D^k_{p_1 p_2}$ requires the least-squares solution of an overdetermined system of linear equations $\mathbf{A}\,\mathbf{x}-\mathbf{B}=\mathbf{E}$, where the coefficient matrix, $\mathbf{A}$, of the linear system depends only on the mesh geometry and can be partially calculated in a preprocessing step. The average solution data at each time step is contained in the matrix, $\mathbf{B}$, and the mean value error in each control volume is in matrix, $\mathbf{E}$, which has the norm minimized in the least-squares sense. Geometric weights of the form $w_J=|\Delta\vec{X}_{IJ}|^{-\theta}$ are assigned to each neighbouring control volume, J, in order to have a more localized reconstruction and improve accuracy for stretched meshes with surface curvature,[78] where $\Delta\vec{X}_{IJ}=\vec{X}_J-\vec{X}_{i,j}$ and values considered herein for the exponent θ are either one or two. Depending on how many solution variables are present in the discretization procedure, the matrices $\mathbf{x}$, $\mathbf{B}$ and $\mathbf{E}$ can have either a single column if there is only one solution variable or more columns for multiple solution variables with each column belonging to one solution unknown. The preservation of the average value, $\bar{u}_{i,j}$, within the reconstructed cell is either explicitly enforced by expressing the coefficient, D^k_{00}, as a function of the other unknowns, a procedure which reduces the dimension of the linear system by one, or by solving a linear equality constrained least-squares problem with the complete set of equations. The former technique provides a faster implementation and it is the preferred one herein.

Both Householder QR factorization algorithm[79] and orthogonal decomposition by SVD method[79] can be used to solve the weighted least-squares problem $\mathbf{A}\,\mathbf{x}-\mathbf{B}=\mathbf{E}$ and determine the polynomial coefficients for all solution variables concurrently, the latter being favoured for the computation of the left pseudo-inverse matrix,[80] $\mathbf{A}^{-1}$, as described below. Note that use of a fixed central stencil here avoids the complexities introduced by performing reconstruction on multiple stencils. In addition, the use of a fixed stencil allows the pseudo-inverse matrix $\mathbf{A}^{-1}$ to be stored and reused for the calculation of *all* solution variables at successive time steps as long as the mesh is not modified. Storage and re-use of the pseudo-inverse was found to reduce significantly the computational costs of performing high-order reconstructions compared to the situation in which the coefficient matrix, $\mathbf{A}$, is formed and the least-squares problem is solved for each spatial reconstruction. Although the procedure based on reusing the pseudo-inverse matrix requires additional storage, the memory requirements are not that substantial and are generally readily available on most modern distributed memory architectures. Thus, the dimensions of the pseudo-inverse matrices encountered herein are 2×8 for linear ($k=1$), 5×24 for quadratic ($k=2$), 9×24 for cubic ($k=3$) and 14×24 for quartic ($k=4$), which corresponds to storing 16, 120, 216 and 336 floating point numbers, respectively. Moreover, these memory requirements do not depend on the number of solution variables since the same pseudo-inverse matrix is employed for the computation of each solution unknown. This procedure therefore represents a practical approach for reducing the cost of the proposed high-order reconstruction and is used here.

To provide concrete examples concerning the condition number, $\kappa(\mathbf{A})$, of the coefficient matrix, $\mathbf{A}$, for the least-squares problem corresponding to different reconstruction orders, k, several representative quadrilateral meshes have been analyzed herein. Thus, Table 1 depicts the maximum values of the condition number based on L_∞ norm of the matrix, $\kappa_\infty(\mathbf{A})=||\mathbf{A}||_\infty\,||\mathbf{A}^{-1}||_\infty$, associated with the linear ($k=1$), quadratic ($k=2$), cubic ($k=3$) and quartic ($k=4$) solution reconstructions on Cartesian grids with aspect ratio, a_r, of 1, 240 and 14,012, respectively, and on two mesh types for the geometry depicted in Fig. 4, a regular smooth mesh and another that is very irregular. The effect of different geometric weighting formulations, w_J, on the condition number has also been considered, and the results are also shown in the table. An analysis of the data in Table 1 reveals that the condition numbers, $\kappa_\infty(\mathbf{A})$, increase with the increase in the reconstruction order, a trend somewhat expected considering how the elements of the coefficient matrix, $\mathbf{A}$, are generated. Additionally, the data shows that larger and larger maximum values occur as the mesh deviates more and more from the Cartesian square grid, the largest values encountered in this study corresponding to the Cartesian grid with the highest aspect ratio. However, the data also reveals that significant improvements in the condition number can be obtained, even up to two orders of magnitude, by using some sort of geometric weighting. For the current scheme and the meshes studied herein it seems that the inverse-distance geometric weighting (i.e., $w_J=|\Delta\vec{X}_{IJ}|^{-1}$) provides the lowest condition number values for all reconstruction orders analyzed. Moreover, although the condition numbers encountered on Cartesian meshes with a high aspect ratio of $a_r=14,012$ are very large, it is argued that a high-order scheme may not require such high aspect ratios to accurately resolve solution features of thin boundary and/or shear layers in practice.

Therefore, it seems that for the reconstruction orders and the meshes considered in this work, the corresponding condition numbers can be dealt with, but caution should be exercised when considering both higher than quartic reconstruction orders or very high grid aspect ratios.

Table 1. The condition numbers of the coefficient matrix, A, obtained based on L_∞ norm of the matrix for different geometric weighting formulations and for several representative meshes, which are as follows: the Cartesian grids with aspect ratio, a_r, of 1, 240 and 14,012; a regular smooth grid and a very irregular grid for the geometry shown in Fig. 4.

Mesh	Geometric Weighting	$\kappa_\infty(\mathbf{A})$			
	$w_J = \lvert\Delta\vec{X}_{IJ}\rvert^{-\theta}$	$k=1$	$k=2$	$k=3$	$k=4$
Cartesian Grid	$\theta=0$	2.0	25.4	452.2	6,748.4
$a_r=1$	$\theta=1$	1.7	22.0	273.2	3,223.8
	$\theta=2$	1.3	32.6	335.3	4,007.2
Cartesian Grid	$\theta=0$	227.6	292,335.1	5.71×10^{8}	9.69×10^{11}
$a_r=240$	$\theta=1$	1.8	1,116.6	1.72×10^{6}	2.01×10^{9}
	$\theta=2$	239.0	245,311.9	3.15×10^{8}	4.03×10^{11}
Cartesian Grid	$\theta=0$	12,780.4	8.40×10^{8}	8.78×10^{13}	1.10×10^{14}
$a_r=14,012$	$\theta=1$	1.8	60,118.4	4.66×10^{9}	9.17×10^{13}
	$\theta=2$	15,047.1	8.32×10^{8}	5.40×10^{13}	2.78×10^{14}
Regular	$\theta=0$	4.1	172.9	9,232.4	524,247.3
Smooth Grid	$\theta=1$	2.2	77.5	3,815.2	171,418.2
	$\theta=2$	3.2	141.9	4,928.2	192,885.6
	$\theta=0$	5.2	191.7	10,552.5	699,826.2
Irregular Grid	$\theta=1$	2.4	84.1	4,661.8	199,873.8
	$\theta=2$	4.6	203.2	6,688.5	240,616.7

III.D.2. Monotonicity Enforcement via Smoothness Indicator

The proposed CENO scheme preserves solution monotonicity in regions of large gradients or discontinuities by reverting the high-order k-exact reconstruction to a limited piecewise linear ($k=1$) reconstruction. This approach of preserving solution monotonicity by "dropping" the reconstruction order leads to a non-uniformly accurate reconstruction (i.e., reconstructions of lower and higher order coexist in the computational domain) for under-resolved and/or non-smooth solution content. However, the reconstruction procedure remains uniformly accurate, even in the presence of smooth extrema, as long as the solution is smooth everywhere. In the current work, the slope limiters of Barth-Jesperson[12] and Venkatakrishnan[81] are used in the limited reconstruction, but other limiters would do almost equally as well. In order to detect regions where the order of the reconstruction should be reduced and the limiters applied, a smoothness indicator is computed for every variable individually within each cell as part of a post-analysis step after the unlimited k-exact reconstruction has been performed. The smoothness indicator is then used in the manner described below to ensure that the limited linear reconstruction is applied to cells with under-resolved and/or non-smooth solution content and the unlimited k-exact reconstruction scheme is where the solution is fully resolved.

The form of the smoothness indicator used here was inspired by the definition of multiple-correlation coefficients that are often used in evaluating the accuracy of curve fits.[79] The basic idea is to assess how accurately the truncated polynomial expansion represents the solution data within the reconstruction stencil. This is achieved by comparing the reconstructed solution to those in neighbouring cells.

The smoothness indicator, $\mathcal{S}$, is calculated in terms of a smoothness parameter, α, as well as information about the number of unknowns (degrees of freedom), DOF, and size of the stencil, SOS, used in the reconstruction. The smoothness indicator, $\mathcal{S}$, and the smoothness parameter, α, are taken to have the form

$$\mathcal{S} = \frac{\alpha}{\max\left((1-\alpha),\epsilon\right)}\frac{(SOS-DOF)}{(DOF-1)}, \qquad \alpha = 1 - \frac{\sum_{\gamma}\sum_{\delta}\left(u^k_{\gamma,\delta}(\vec{\bar{r}}_{\gamma,\delta}) - u^k_{i,j}(\vec{\bar{r}}_{\gamma,\delta})\right)^2}{\sum_{\gamma}\sum_{\delta}\left(u^k_{\gamma,\delta}(\vec{\bar{r}}_{\gamma,\delta}) - \bar{u}_{i,j}\right)^2}, \tag{9}$$

where the ranges of the indices, γ and δ, are taken to include all control volumes in the reconstruction stencil for cell (i,j), $\vec{\bar{r}}_{\gamma,\delta}$ is the centroid of the cell (γ,δ), and the tolerance, ϵ, has been introduced in order to avoid division by zero. A suitable value for ϵ has been found to be 10^{-8}. It should be evident that the parameter, α, compares the values of the reconstructed solution at the centroids of neighbouring cells used in the solution reconstruction for cell (i,j). Note also that the average value in the reconstructed cell is

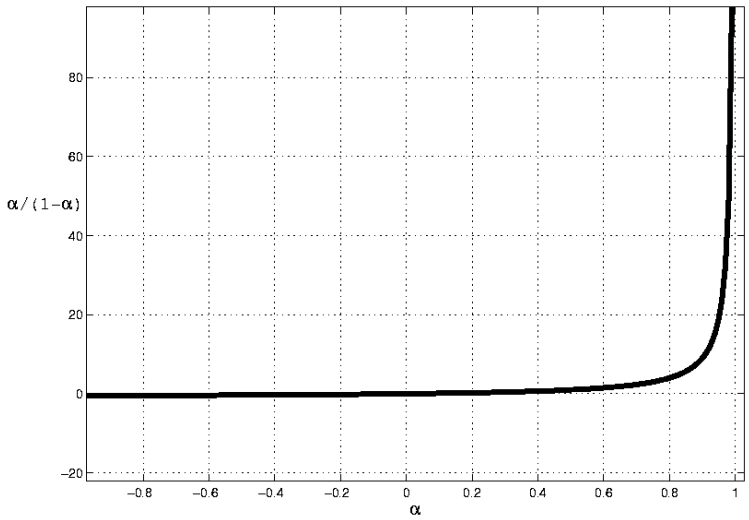

Figure 2. The graph of $f(\alpha) = \frac{\alpha}{(1-\alpha)}$.

used to normalize the relative predictions of the reconstructions. The range for α is $-\infty < \alpha \leq 1$ and it will approach unity as the solution becomes smooth and near perfect matching of the reconstructions in adjacent cells is achieved. The quotient in the expression for α can become a ratio of two very small numbers or $\frac{0}{0}$ in situations with little or no solution variation encountered. This scenario would translate into the problem that reconstructions of free-stream conditions are not deemed as smooth and a second reconstruction would be required in these regions. Obviously, such situations can be easily avoided by computing α only in those regions of the domain where a minimum level of solution variation relative to a reference solution value is encountered. The variation of $\frac{\alpha}{(1-\alpha)}$ is depicted in Fig. 2 and the figure shows that $\mathcal{S}$ rapidly becomes large as α approaches unity.

Once evaluated, the smoothness indicator, $\mathcal{S}$, is then compared to a pass/no-pass cutoff value, $\mathcal{S}_c$. As appropriate value for the cutoff was determined from a wide range of numerical experiments and values for $\mathcal{S}_c$ in the range 1,000-5,000 seem to work well. It should be pointed out that smoothness indicators for smooth solutions are typically orders of magnitude larger than the range of cutoff values (e.g., 100,000). Moreover, typical values for cells located in the "middle" of discontinuities are close to 10. Thus for $\mathcal{S} < \mathcal{S}_c$, the solution is deemed to be under-resolved and/or non-smooth and the high-order k-exact reconstruction is replaced by limited linear reconstruction in that cell. For $\mathcal{S} > \mathcal{S}_c$, the unlimited high-order reconstruction is deemed to be acceptable and retained. Additionally, the solution procedure of Euler and Navier-Stokes equations that is based on the high-order reconstruction of the conserved variables should enforce positivity of density and pressure by performing a limited reconstruction of the primitive variables in those regions detected as non-smooth based on the conserved ones. Finally, it should be pointed out that the effect of a reconstruction which contains discontinuous data is reflected in the smoothness indicator calculation of few neighbours and consequently, any solution discontinuity is typically confined to within at most 7 to 10 cells.

III.D.3. Reconstruction at Boundaries and Implementation of High-Order Boundary Conditions

Correct high-order treatment of boundary conditions is a crucial element for developing accurate numerical schemes. It is especially important for high-order methods, where errors due to geometrical approximation may dominate the discretization error, mitigating the full capabilities of a high-order scheme. One approach to imposing high-order BCs is to make use of extra rows of ghost cells which are added beyond the geometric boundary of the computational domain. Solution states are then imposed in the ghost cells in such a way that the reconstructed solution and/or flux at the boundary flux interior cell approximates those associated with the particular boundary condition. An alternative approach is to enforce the boundary conditions by constraining the least-squares reconstruction in control volumes adjacent to the boundary as described by Olivier-Gooch and Van Altena.[51] In the current work, both procedures (i.e., ghost cells and constrained reconstruction) for boundary-condition prescription have been implemented and are described herein.

In order to obtain high-order accuracy at boundaries, the geometric data (i.e., cell area, centroid, geometric moments, normals, edge lengths, locations of the Gauss quadrature integration points) are computed

to the same order of accuracy as that of the interior scheme.

Implementing BCs with additional layers of ghost cells can work well for relatively straight boundaries, but may give rise to large errors when the geometry is more highly curved. The difficulty consists in specifying accurate solution information in the ghost cells which then translates to accurate high-order reconstructions that correctly resemble the solution variation required for the particular boundary condition. A better alternative is to enforce the BCs using only information from the interior domain and from the required boundary values at the Gauss integration points along the boundary. Thus, additional constraints are added to the reconstruction procedure to ensure that the values taken by the polynomial approximations of the interior cells next to the boundary at the Gauss integration points are exactly those required by the particular boundary condition. By constraining the least-squares reconstruction in control volumes adjacent to the boundary, complex boundary conditions can be enforced. In particular, two basic types of constraints have been applied in this work: 1) Robin (i.e., linear combination of Dirichlet and Neumann) conditions which can be applied individually to any reconstructed variable as the need may be; and 2) linear relations among variables which are applied as coupling constraints to a set of reconstructed variables. Nevertheless, for certain boundary conditions the constrained reconstruction approach might be too difficult, and therefore, in the current implementation both procedures (i.e., ghost cells and constrained reconstruction) are allowed.

Similarly to the derivation outlined in,[51] the general constraint equation which must be satisfied at a flux calculation point, $\vec{X}_g$, to impose Robin BCs in terms of the cell reconstruction, $u^k(\vec{X})$, can be expressed as

$$\begin{aligned} f(\vec{X}_g) &= f(a,b,f_D,f_N)\Big|_{\vec{X}_g} \\ &= \sum_{\substack{p_1=0 \\ (p_1+p_2\leq k)}}^{k}\sum_{p_2=0}^{k}\left\{\Delta X_g^{(p_1-1)}\ \Delta Y_g^{(p_2-1)}\left[a\ \Delta X_g\ \Delta Y_g + b\ p_1\ \Delta Y_g\ n_x^g + b\ p_2\ \Delta X_g\ n_y^g\right]\right\} D^k_{p_1p_2} \end{aligned} \tag{10}$$

where $\Delta X_g = x_g - \bar{x}_{i,j}$, $\Delta Y_g = y_g - \bar{y}_{i,j}$, and $\vec{n}^g(n_x^g, n_y^g)$ is the normal unit vector at the point $\vec{X}_g$. The function $f(a,b,f_D,f_N,\vec{X}) = a(\vec{X})\,f_D(\vec{X}) + b(\vec{X})\,f_N(\vec{X})$ provides the value of the Robin BC at each location $\vec{X}$ of interest. The coefficients $a(\vec{X})$ and $b(\vec{X})$ define the contribution of the Dirichlet, $f_D = u(\vec{X})$, and Neumann, $f_N = \frac{\partial u(\vec{X})}{\partial n}$, components respectively. The values of $f(a,b,f_D,f_N,\vec{X})$ are entries in the matrix $\mathbf{B}$ of the linear system, as they are known at each integration point. Equation 10 is valid for any reconstruction order k and the general term between braces can be used directly to generate the entries corresponding to any combination of p_1 and p_2 in the matrix $\mathbf{A}$ of the linear system for a particular integration point, $\vec{X}_g$.

An example of coupled constraints is the implementation of inviscid solid wall condition or zero-shear slip wall in viscous flows (i.e., symmetry plane BC), $\vec{V}\cdot\vec{n} = 0$, which is imposed by solving a coupled constrained reconstruction with the velocity components and requiring that the velocity vector is tangent to the geometry at every Gauss integration point. Thus, the equation that needs to be satisfied by the reconstruction coefficients of the x- and the y-velocity components, $(D^k_{p_1p_2})_u$ and $(D^k_{p_1p_2})_v$ respectively, is

$$\sum_{\substack{p_1=0 \\ (p_1+p_2\leq k)}}^{k}\sum_{p_2=0}^{k}\Delta X_g^{p_1}\ \Delta Y_g^{p_2}\ n_x^g (D^k_{p_1p_2})_u + \sum_{\substack{p_1=0 \\ (p_1+p_2\leq k)}}^{k}\sum_{p_2=0}^{k}\Delta X_g^{p_1}\ \Delta Y_g^{p_2}\ n_y^g (D^k_{p_1p_2})_v = 0\ . \tag{11}$$

The matrix $\mathbf{A}$ for a constrained least-squares reconstruction in which two variables are coupled contains entries for the relational constraints, for the individual constraints of each variable and for the exactly and approximately satisfied mean conservation equations provided by the reconstructed cell and the neighbours that are part of the stencil, respectively. To solve the constrained least-squares problem, Gauss elimination algorithm with pivoting can be applied to eliminate the constraints followed by the application of any of the aforementioned algorithms to minimize the error in the least-squares sense for the rest of the equations.

The constrained reconstruction approach has been applied to Euler and Navier-Stokes equations by selecting the variables to be constrained such that to satisfy the particular boundary condition while maintaining a well-posed mathematical problem. Note that for hyperbolic problems an upwind consistent selection of the constrained variables is also possible by estimating the flow direction as described by Gottlieb and Groth.[82]

III.E. Inviscid (Hyperbolic) and Viscous (Elliptic) Flux Evaluation

An upwinding formulation is used herein to evaluate the hyperbolic flux at each integration point. Thus, the hyperbolic flux in the advection-diffusion equation, Eq. (1), at a quadrature point is given by

$$\vec{F}_H \cdot \vec{n} = \begin{cases} u_l \left(\vec{V} \cdot \vec{n}\right) & \text{if } \vec{V} \cdot \vec{n} \geq 0, \\ u_r \left(\vec{V} \cdot \vec{n}\right) & \text{if } \vec{V} \cdot \vec{n} < 0, \end{cases} \tag{12}$$

where the left and right solution states, u_l and u_r, at the inter-cellular face are determined by performing piecewise k-order CENO solution reconstruction within each computational cell, as outlined in Sect. III.D.

For the Euler and the Navier-Stokes equations, the inviscid numerical flux, $\vec{\mathbf{F}}_{\mathrm{H}} \cdot \vec{n}$, at the quadrature points is given by $\vec{\mathbf{F}}_{\mathrm{H}} \cdot \vec{n} = \mathcal{F}(\mathbf{U}_l, \mathbf{U}_r, \vec{n})$, where the numerical flux $\mathcal{F}$ is evaluated by solving a Riemann problem in a direction defined by the normal to the face with initial data given by the left, $\mathbf{U}_l$, and right, $\mathbf{U}_r$, high-order solution states. In the present algorithm, both exact and approximate Riemann solvers can be used to solve the Riemann problem and evaluate the numerical flux. In particular, the linearized Roe Riemann solver,[83] HLLE and modified HLLE flux function due to Linde,[84–86] and the exact Riemann solver of Gottlieb and Groth[82] have all been implemented for systems of equations and may be used.

In a similar manner to hyperbolic fluxes, numerical elliptic fluxes in the advection-diffusion equation given by Eq. (1), $\vec{F}_E \cdot \vec{n} = -\kappa \, \vec{\nabla} u \cdot \vec{n}$, must be evaluated at each quadrature point of each control volume face. Having determined the left and right $(k+1)$-order accurate scalar solution reconstructions, $u_l^k(\vec{X})$ and $u_r^k(\vec{X})$, a k-order accurate solution gradient at the inter-cellular face is obtained as the arithmetic mean of the left and right reconstruction gradients and thus, the elliptic flux at the calculation point, $\vec{X}$, is evaluated as $\vec{F_E} \cdot \vec{n} = -\kappa \, \left[\frac{1}{2} \left(\vec{\nabla} u_l^k(\vec{X}) + \vec{\nabla} u_r^k(\vec{X})\right)\right] \cdot \vec{n}$. Similarly, numerical diffusion fluxes in the Navier-Stokes equations are evaluated as $\vec{\mathbf{F}}_{\mathrm{E}} \cdot \vec{n} = \vec{\mathbf{F}}_{\mathrm{E}} \left(\mathbf{U}, \vec{\nabla}\mathbf{U}\right) \cdot \vec{n} = \vec{\mathbf{F}}_{\mathrm{E}} \left(\frac{1}{2} \left(\mathbf{U}_l^k(\vec{X}) + \mathbf{U}_r^k(\vec{X})\right), \frac{1}{2} \left(\vec{\nabla}\mathbf{U}_l^k(\vec{X}) + \vec{\nabla}\mathbf{U}_r^k(\vec{X})\right)\right) \cdot \vec{n}$, where the 2D reconstruction gradient, $\vec{\nabla}\mathbf{U}^k$, at a given location $\vec{X}$ is given by $\vec{\nabla}\mathbf{U}^k(\vec{X}) = \left.\frac{\partial U^k}{\partial x}\right|_{\vec{X}} \hat{\imath} + \left.\frac{\partial U^k}{\partial y}\right|_{\vec{X}} \hat{\jmath}$. In the gradient expression, $\hat{\imath}$ and $\hat{\jmath}$ are the Cartesian unit vectors and the derivative of the reconstructed polynomial in the x- and y-direction, $\frac{\partial U^k}{\partial x}$ and $\frac{\partial U^k}{\partial y}$, respectively, are computed based on the polynomial coefficients as

$$\left.\frac{\partial U^k}{\partial x}\right|_{\vec{X}} = \sum_{\substack{p_1=0 \\ (p_1+p_2 \neq 0)}}^{k} \sum_{p_2=0}^{k} p_1 (x - \bar{x}_{i,j})^{p_1 - 1} (y - \bar{y}_{i,j})^{p_2} D^k_{p_1 p_2} \, , \tag{13a}$$

$$\left.\frac{\partial U^k}{\partial y}\right|_{\vec{X}} = \sum_{\substack{p_1=0 \\ (p_1+p_2 \neq 0)}}^{k} \sum_{p_2=0}^{k} p_2 (x - \bar{x}_{i,j})^{p_1} (y - \bar{y}_{i,j})^{p_2 - 1} D^k_{p_1 p_2} \, . \tag{13b}$$

Clearly, computing the interface gradients by averaging the reconstructions used for the discretization of hyperbolic operators, as described above, has important computational advantages but it also raises questions about its usability, as similar formulations with second-order discretizations lead to several problems such as odd-even solution decoupling.[43, 87] To shed some light on whether the current elliptic discretization suffers from any of the problems reported in the literature, a series of investigations have been performed for different reconstruction orders. While the accuracy of the interface gradient can be readily observed to be k-order accurate based on the design of the scheme, other properties of the resulting discretization such as positivity (related to local satisfaction of a discrete maximum principle) or odd-even solution decoupling can be only inferred from more careful analysis.

For these purposes, it is convenient to apply the proposed elliptic discretization to the Laplace operator, $L(u) = \nabla^2 u$, and analyze the influence coefficient (i.e., the weight) of each entry in the supporting stencil.[43] Hence, the sufficient condition for the discrete local Laplacian based on an N-point stencil, $\tilde{L}(u) = \sum_{n=0}^{N} \alpha_n \bar{u}_n$, to satisfy a discrete version of the maximum principle is to require that all weights satisfy $\alpha_n \geq 0$ for $n \in [1, N]$. For a given elliptic discretization scheme and a supporting stencil the weights, α_n, and consequently the positivity of the scheme, depend only on the local mesh geometry and not on the actual solution. For

arbitrary mesh geometries, a convenient and more generic way to compute the weights, α_n, is by a finite-differencing approximation. As proposed by Coirier,[43] the positivity and stability of the scheme can then be characterized in terms of α_0 and $\tilde{\alpha}_{\min}$ coefficients. Ideally, $\alpha_0 < 0$ for stability and $\tilde{\alpha}_{\min} = 0$ for positivity.[44]

In the current work, different mesh topologies were analyzed including Cartesian, stretched, and randomly disturbed quadrilateral grids. Analysis of the proposed discretization procedure has shown that odd-even solution decoupling does not occur. In terms of the stability and positivity, it was found that $\alpha_0 < 0$ (i.e., the schemes are stable) but also $\tilde{\alpha}_{\min} < 0$ for discretizations of all order, unfortunately implying that, while stable, none of the discretizations satisfy the discrete maximum principle. This result agrees with the general perception that, for finite-volume discretizations, accuracy and positivity are essentially conflicting properties.[43] Note that for square Cartesian meshes, values for $\tilde{\alpha}_{\min}$ are found to be -0.823 for $k=2$, -0.362 for $k=3$ and -0.854 for $k=4$ when inverse distance geometric weighting is used in the k-exact reconstruction. However, the positivity can be improved by using an inverse distance squared geometric weighting, for which $\tilde{\alpha}_{\min}$ was found to be -0.051 for $k=2$, -0.247 for $k=3$ and -0.324 for $k=4$. For non-Cartesian meshes, large variations in the value of $\tilde{\alpha}_{\min}$ are possible ($-5 < \tilde{\alpha}_{\min} < 0$), depending on the regularity and topology of the mesh. It should be mentioned that for the test problems and the computational meshes discussed in Sect. V, the lack of strict positivity of the elliptic discretization did not seem to represent an obvious issue.

IV. High-Order CENO with Parallel Adaptive Mesh Refinement

The implementation of the proposed adaptive high-order CENO finite-volume algorithm is considered using the block-based AMR framework proposed and developed by Sachdev *et al.*,[57] Gao and Groth,[62,88] and Gao *et al.*[89] for body-fitted mesh. Thus, a flexible block-based hierarchical data structure is used in conjunction with the CENO finite-volume scheme to facilitate automatic solution-directed mesh adaptation on 2D body-fitted multi-block quadrilateral mesh. The method allows for the use of anisotropic mesh and is well suited to parallel implementation via domain decomposition. In contrast to the lower-order variant, the high-order mesh adaptation procedure described herein requires the development of inter-block communication dependent on the order of solution accuracy and formulation of high-order treatment of physical boundaries, boundary conditions and solution transfer between AMR grids. Aspects of the block-based AMR algorithm for multi-block quadrilateral mesh and second-order finite-volume method are described in the work by Sachdev *et al.*,[57] and the approach has been already successfully applied to the prediction of various complex flows.[60–62] Moreover, the combination of high-order CENO with this AMR strategy has been already investigated by Ivan and Groth for inviscid flow simulation,[56] and is considered for application to viscous flow problems herein. As such, this section outlines the important elements of the high-order solution-adaptive computational framework for the sake of completeness, while the rest of details are provided in.[56,77]

In the block-based AMR algorithm considered herein, mesh adaptation is accomplished by the dividing and coarsening of appropriate solution blocks. In regions requiring increased cell resolution, a "parent" block is refined by dividing itself into four "children" or "offspring". Each of the four quadrants or sectors of a parent block becomes a new block having the same number of cells as the parent and thereby doubling the cell resolution in the region of interest. This process can be reversed in regions that are deemed over-resolved and four children are coarsened into a single parent block. The mesh refinement is constrained such that the grid resolution changes by only a factor of two between adjacent blocks. A hierarchical tree-like data structure with multiple "roots", multiple "trees", and additional interconnects between the "leaves" of the trees is used to keep track of mesh refinement and the connectivity between solution blocks.

In the refinement process of a grid block the geometry of the newly created cells belonging to the offspring is obtained by dividing the domain of each coarse interior cell into four fine cells denoted as I, II, III and IV, as illustrated in Fig. 3. The new nodes represent the midpoint of each coarse face and the weighted average of the four coarse corners. Note that a body-fitted mesh is simply obtained herein by ensuring that the inserted points are on the boundary splines representing the physical curved boundaries. Note also that the utilization of high-order boundary elements (i.e., curved-edge quadrilaterals) for curved boundaries, as seen in Fig. 3(b), ensures naturally the equality of the coarse element area, A_Ω, and the summation area of the offspring. Based on this property, the solution conservation equation $\bar{u}_\Omega A_\Omega = \bar{u}_I A_I + \bar{u}_{II} A_{II} + \bar{u}_{III} A_{III} + \bar{u}_{IV} A_{IV}$ can be written for each average conserved solution quantity, $\bar{u}_\Omega$, of the coarse cell.

The hybrid CENO solution reconstruction procedure is used in conjunction with standard multi-grid-type restriction and prolongation operators to evaluate the solution on all blocks created by the coarsening and

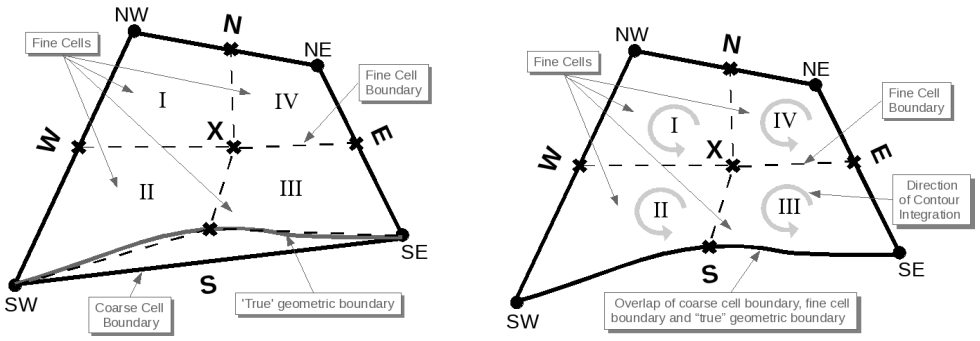

(a) Low-order boundary representation (b) High-order boundary representation

Figure 3. Depiction of a coarse cell division into four fine cells for low- and high-order block boundary elements.

division processes, respectively. The restriction and prolongation operators used herein are derived from the conservation property of the solution content for overlapping cell domains. Additionally, a high-order accurate solution transfer from the coarse cell to the fine cells (i.e. prolongation) is provided here by incorporating information about the solution distribution over the coarse cell domain. In particular, to distribute the average solution quantity among offspring with high-order accuracy the high-order polynomial reconstructions of all solution variables in the coarse cell are integrated over the domain of each fine cell. Although this prolongation operator automatically conserves the average solution of the coarse cell, $\bar{u}_\Omega$, it does not enforce explicitly the positivity conditions, such as non-negative pressure and density, and consequently, in case they are violated, a direct injection approach (i.e., $\bar{u}_I = \bar{u}_{II} = \bar{u}_{III} = \bar{u}_{IV} = \bar{u}_\Omega$) is used herein.

For reconstructions performed with derived quantities such as primitive solution states, $\bar{W}$, the approach considered in this work is to compute the average conserved state of each fine cell by correcting the average quantities, $f\left(\bar{W}_i'\right)$, obtained from integration of the coarse reconstruction polynomials with any non-zero solution error distributed uniformly over the coarse cell domain. Thus, the average conserved solution state for a fine cell s is given by

$$\bar{U}_s = \bar{U}_s' + \Delta\bar{U} = f\left(\bar{W}_s'\right) + \frac{1}{A_\Omega}\left[\bar{U}_\Omega A_\Omega - \sum_{i=I}^{IV} f\left(\bar{W}_i'\right) A_i\right], \tag{14}$$

where $f(W)$ represent the mapping function of the derived quantities into the conserved ones. As in the previous case, direct injection is used if non-physical values are encountered.

In order that the finite-volume scheme can be applied to all blocks in a more independent manner, some solution information is shared between adjacent blocks having common interfaces. This information is stored in additional layers of overlapping "ghost" cells associated with each block. Within the AMR approach, additional inter-block communication is also required at interfaces with resolution changes to strictly enforce the flux conservation properties of the finite-volume scheme.[90,91] In particular, the interface fluxes computed on more refined blocks are used to correct the interface fluxes computed on coarser neighbouring blocks and ensure the solution fluxes are conserved across block interfaces.

In previous work, the coarsening and division of blocks was directed using multiple physics-based refinement criteria.[57,60–62] In this work, an h-refinement criterion based on the solution smoothness indicator is defined and used to control refinement of the body-fitted multi-block AMR mesh. The form considered herein for the CENO-based refinement criterion is $\mathcal{R}_c = e^{-\frac{\max(0,\mathcal{S})}{\mathcal{U}_s * \mathcal{S}_c}}$, where $\mathcal{U}_s$ is a scaling coefficient. Note that the proposed refinement criterion is non-dimensional and consequently, the relative importance of different variables for AMR can be easily assessed based only on their relative smoothness. Further details about the h-refinement criterion can be found in.[56,77]

Although the block-based AMR approach described above is somewhat less flexible and incurs some inefficiencies in solution resolution as compared to a cell-based approaches (i.e., for the same solution accuracy, generally more computational cells are introduced in the adapted grid), the block-based method offers many advantages over cell-based techniques when parallel implementation of the solution algorithm is considered and computational performance issues are taken into account. In particular, the multi-block quadrilateral mesh and quadtree data structure lends itself naturally to geometric domain decomposition as the solution blocks can be easily distributed to the processors, with more than one block permitted on each processor. Thereby, it should enable efficient and scalable implementations of the CENO finite-volume scheme on

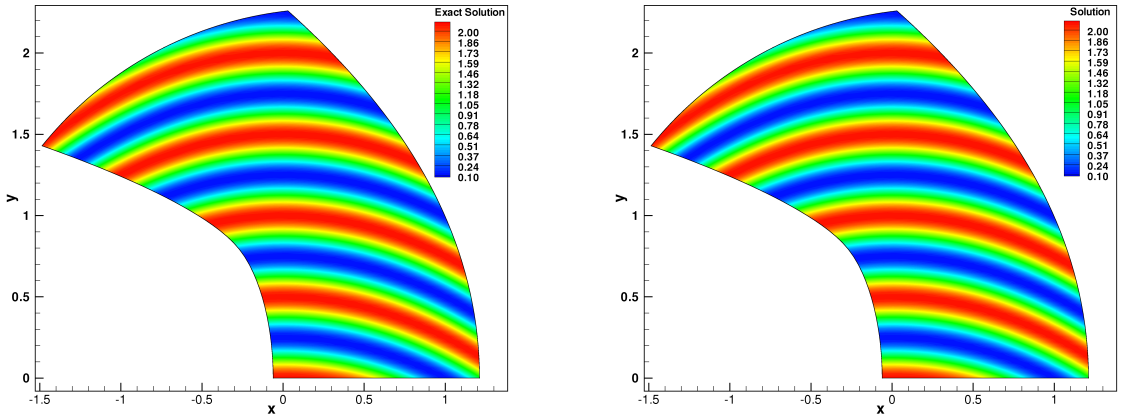

(a) Exact solution

(b) Quartic ($k=4$) solution reconstruction

Figure 4. Exact solution of function $u(x,y) = 1.1 + \cos(\pi x^2 + 4\pi y)$ and the quartic solution reconstruction on a regular mesh with 40×40 computational cells.

distributed-memory homogeneous multi-processor (identical processors) architectures, as demonstrated for various 2nd-order algorithms.[57,60–62] The parallel efficiency for the proposed high-order CENO scheme is examined in Sect. V.G.1.

V. Numerical Results

To demonstrate the capabilities of the proposed high-order CENO scheme described herein, numerical results are now presented for solution reconstruction in two-space dimensions, as well as for various two-dimensional flow problems governed by the advection-diffusion and the Navier-Stokes equations. Moreover, the influence of different solution sets of reconstruction variables on the accuracy of the CENO scheme is assessed based on Ringleb's flow. Furthermore, the predictive capabilities of the CENO scheme are illustrated with results on both fixed and AMR meshes.

V.A. Reconstruction of a Two-Dimensional Smooth Trigonometric Function

The properties of the CENO reconstruction for two-dimensional smooth solution variations are now illustrated with the trigonometric function $u(x,y) = 1.1+\cos(\pi x^2+4\pi y)$ and the domain defined by the Ringleb's flow[92] solution between the streamlines corresponding to $k = 0.75$ and $k = 1.5$, and the iso-velocity contour $q = 0.5$ (see Sect. V.F for more details about the Ringleb's flow). The exact solution for this problem and the quartic ($k=4$) CENO reconstructed solution on a regular mesh with 40×40 cells are shown in Fig. 4. As can be easily observed, the quartic CENO reconstruction captures all the smooth extrema of the function very well on this relatively coarse mesh, generating a solution profile that is visually indistinguishable from the exact solution. Note also that the solution gradients are not at all aligned with the mesh in this test.

To quantify the errors of the CENO reconstruction procedure for this problem convergence studies have been carried out with different parameters and two types of meshes ranging from 10×10 to 160×160 computational elements. The first sequence of meshes was represented by regular grids whereas the second sequence was generated by disturbing randomly the nodes of the meshes in the first category. The perturbed mesh with 40×40 computational cells used for this study is shown in Fig. 5(a). To evaluate the accuracy of the CENO procedure the cubic ($k=3$) and quartic ($k=4$) reconstructions have been considered in three cases: A) using only k-exact reconstruction, B) using CENO reconstruction with a pass/no-pass cutoff value $\mathcal{S}_c = 1,000$ and C) using CENO reconstruction with $\mathcal{S}_c = 5,000$. In Fig. 5 the corresponding convergence history in all these situations is presented for L_1, L_2, and L_∞ error norms. The results verify that the theoretical convergence orders based on different error norms which are four for the cubic and five for the quartic reconstruction, respectively, are achieved at least in the asymptotic limit. Additionally, the error norms obtained on the disturbed meshes are very similar to those corresponding to the regular grids, although the absolute error is slightly larger, and they are both very close to the asymptotic convergence rates indicated with the triangles depicted in the figures.

The influence of the cutoff value, $\mathcal{S}_c$, can also be inferred from the plots. First, note that all considered

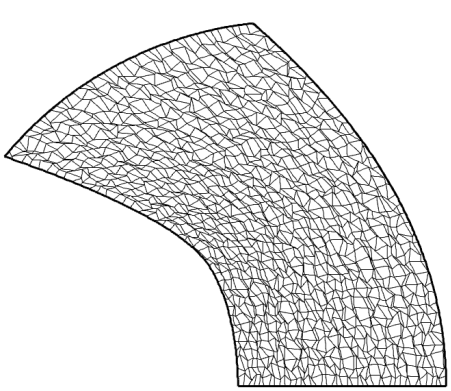

(a) An irregular grid with 40×40 cells

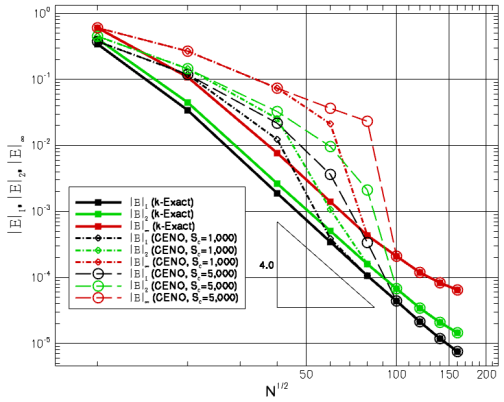

(b) Cubic ($k=3$) reconstruction on regular mesh

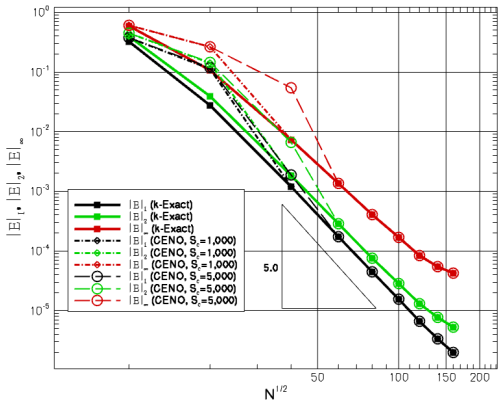

(c) Quartic ($k=4$) reconstruction on regular mesh

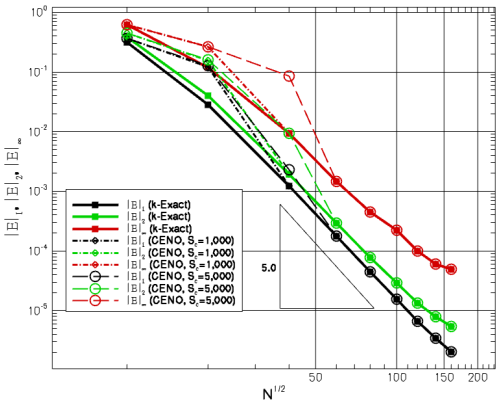

(d) Quartic reconstruction on disturbed mesh

Figure 5. Cubic and quartic convergence history for L_1, L_2, and L_∞-norms of the reconstruction error of the function $u(x,y) = 1.1 + \cos(\pi x^2 + 4\pi y)$. Three cases are considered based on the cutoff value, $\mathcal{S}_c$: A) k-exact, B) $\mathcal{S}_c = 1,000$ and C) $\mathcal{S}_c = 5,000$. The irregular grid with 40×40 cells used in this study is shown in (a).

reconstructions produce similar errors on a mesh with 10×10 cells regardless of the cutoff value which confirms the fact that this mesh is well under-resolved. Next, a "transition" regime occurs in which not all cell reconstructions are considered resolved based on the cutoff value and differences between the k-exact and the CENO errors are observed. The extent of this transition regime is a function of the cutoff value but also of the order of the reconstruction, as can be seen be comparing the plots in Fig. 5(b) and (c). Finally, after a minimum resolution has been attained and all cell reconstructions are deemed to be smooth, the solution maintains only the character of the k-exact reconstruction and becomes insensitive to cutoff values in the recommended range (i.e. 1,000-5,000). Note that for the complex solution variation considered herein and a cubic reconstruction, the minimum resolution corresponds to around 60 to 100 cells in one-space dimension. However, the quartic reconstruction is able to capture more accurately the inflections of the tested function with fewer cells and consequently, enters into the final regime at a minimum resolution of around 40 to 60 cells.

V.B. Residual-Based Accuracy Assessment for Poisson Equation

To investigate the accuracy of the proposed algorithm for discretization of elliptic operators, convergence studies based on the residual error to Poisson equation $\vec{\nabla}\cdot(\vec{\nabla}u) = a\, e^{\beta\, u}$ have been performed using the exact solution $u(x,y) = \frac{1}{\beta}\left[\ln\left(\frac{8C}{a\beta}\right) - 2\ln|(x+A)^2 + (y+B)^2 - C|\right]$, where $A=2.0$, $B=1.0$, $C=2.0$, $a=2.5$ and $\beta=0.001$. The domain in this study was the rectangular box defined by $0.5\le x,y\le 4.5$. The L_1, L_2 and L_∞ norms of the flux integral (i.e. the residual) errors obtained for a sequence of Cartesian and randomly disturbed meshes are shown in Fig. 6(a) and (b), respectively, for quadratic ($k=2$), cubic ($k=3$) and quartic ($k=4$) interpolants. The correspondent slopes of the L_1-, L_2- and L_∞-norms were determined based on all measured error values and are shown in Table 2 for both Cartesian and disturbed meshes.

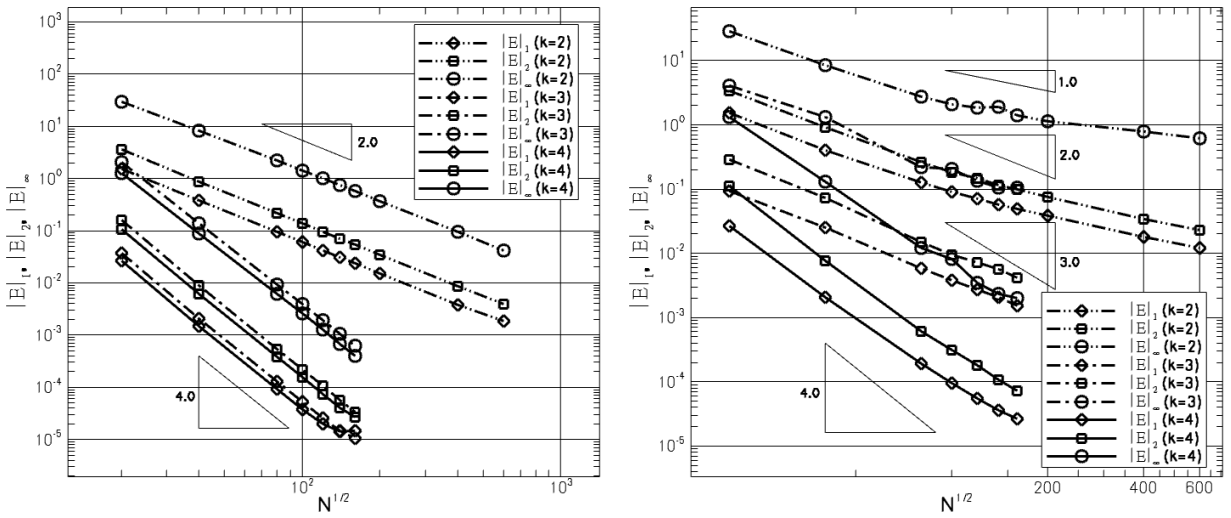

(a) Error norms for Cartesian meshes

(b) Error norms for distorted meshes

Figure 6. L_1, L_2 **and** L_∞ **norms of the residual error to Poisson equation** $\vec{\nabla} \cdot (\vec{\nabla} u) = a\, e^{\beta u}$ **for piecewise quadratic (**$k=2$**), cubic (**$k=3$**) and quartic (**$k=4$**) reconstructions versus the number of computational cells of (a) Cartesian meshes and (b) randomly distorted meshes.**

Table 2. The slope values corresponding to each convergence error plot shown in Fig. 6.

Mesh	Reconstruction Order	L_1	L_2	L_∞
Cartesian Grid	$k=2$	1.99	2.01	1.93
	$k=3$	3.98	4.07	3.89
	$k=4$	3.77	4.02	3.87
Distorted Grid	$k=2$	1.41	1.47	1.10
	$k=3$	1.99	2.05	1.86
	$k=4$	3.35	3.53	3.18

The results of Fig. 6 and Table 2 show that both cubic and quartic interpolants produce a 4th-order scheme for Cartesian meshes in all error norms, whereas the quadratic reconstruction generates a 2nd-order one. The result for $k=3$ in Fig. 6(a) demonstrates that due to error cancellations a cubic interpolant is also able to generate a 4th-order scheme for elliptic operator discretizations. However, an analysis of the error norms in Fig. 6(b) reveals that the error cancellation effect does not occur on the randomly disturbed meshes and as such, the error norms of cubic and quartic reconstructions differ by more than one unit. Unfortunately, this is not a rigorous convergence study due to the random disturbance of the nodes and as a result, the error norms of both reconstructions are somewhat lower than the expected theoretical ones. However, the numerical results provide support for the point made concerning the effects of error cancellation.

V.C. Solution of the Laplace Equation on Curved Boundaries

The numerical scheme was also investigated for solutions to the Laplace equation and geometries with curved boundaries such as the annulus domain shown in Fig. 7(a). Dirichlet boundary conditions were implemented along the domain contour based on the exact solution considered for this problem which was $u(x,y) = e^{\mu x}\,(A\,\cos(\mu\, y) + B\,\sin(\mu\, y))$, where $A=1$, $B=2$ and $\mu=1.5$. The predicted solution obtained using the 4th-order ($k=4$) high-order scheme on a curvilinear mesh with 40×40 cells is shown in Fig. 7(a). The L_1, L_2, and L_∞ norms of the error in the predicted solution for cubic ($k=3$) and quartic ($k=4$) interpolants are given in Fig. 7(b) for this problem. The slopes of the L_1- and L_2-norms reach in the asymptotic limit -3.86 and -3.85 for $k=3$ and -3.86 and -3.81 for $k=4$, respectively. As can be easily observed, even if the slope of the cubic and quartic polynomials are basically the same and both very close to the theoretical value, there is about one order difference between the magnitudes of the errors, demonstrating the benefits

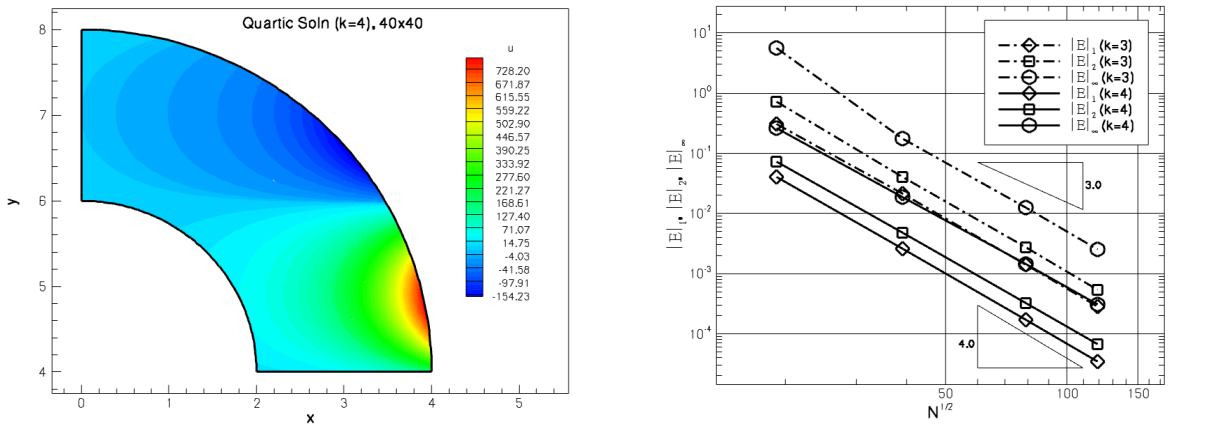

(a) (b)

Figure 7. (a) Fourth-order ($k=4$) solution to the Laplace equation on a mesh with 40×40 computational cells. (b) L_1, L_2 and L_∞ norms of the error as a function of mesh density obtained with the cubic ($k=3$) and quartic ($k=4$) polynomial interpolants.

of using quartic interpolants.

V.D. Two-Dimensional Channel Flow Problem on Fixed Mesh

The application of the proposed CENO scheme is now considered for problems involving both advection and diffusion terms for a range of Péclet numbers. Solution of the advection-diffusion equation Eq. (1) with a constant velocity, $\vec{V}=(v_0,0)$, and constant diffusion coefficient, $\kappa(x,y)=\kappa_0=0.01$, on the rectangular domain of length $L=3$ and unit width was considered for three different Péclet numbers, depending on the value of v_0. The studied Péclet numbers correspond to Pe$=0.1$, at which diffusion dominates the flow, to Pe$=1$, at which advection and diffusion are equally represented and to Pe$=10$, which is representative for an advection dominated problem.

The BCs for this problem, as shown in Fig. 8, are: $u(x,0)=u(x,1)=0$, $u(0,y)=\sin(\pi\,y)$ and $\frac{\partial u(L,y)}{\partial x}=0$. A similar study was considered by Ollivier-Gooch and Van Altena for the evaluation of high-order finite-volume schemes in.[51] The analytic solution to this problem can be determined by the method of separation of variables and can be arranged such that to avoid numerical problems for convection dominated flows in the form $u(x,y)=\frac{\sin(\pi\,y)}{\left(R\left[e^{L(R-1)}\right]^{r_1}-1\right)}\left(R\left[e^{(R\,L+x-L)}\right]^{r_1}-e^{r_2\,x}\right)$, where $r_{1,2}=\frac{v_0}{2\,\kappa_0}\pm\sqrt{\frac{v_0^2}{4\,\kappa_0^2}+\pi^2}$ and $R=\frac{r2}{r1}$.

The numerical solution obtained for Pe$=10$ on an 80×40 Cartesian mesh is shown in Fig. 8(a) and the error norms for this advection-diffusion problem associated to each of the three Péclet numbers are shown in Fig. 8(b)–(d). The results show that the errors generated by the quartic polynomial are consistently lower than those of the cubic interpolant by at least one order of magnitude for all Péclet numbers and get the theoretical accuracy in all norms. Thus, the L_1- and L_2-norms for $k=4$ are -4.02 and -4.08 for Pe$=0.1$, -4.30 and -4.46 for Pe$=1.0$ and -3.92 and -3.95 for Pe$=10.0$, respectively. In the case of cubic interpolant, the error norms are -3.92 and -3.85 for Pe$=0.1$, -3.88 and -3.81 for Pe$=1.0$ and -3.53 and -3.62 for Pe$=10.0$, respectively. It can be also seen in the error plots that, for the same accuracy level, the cubic interpolant requires almost twice as many computational cells as the quartic one. Taking into account that both polynomial reconstructions, quartic and cubic, use the same reconstruction stencil, the only extra cost associated with quartic reconstruction is to determine five additional variables during the least-squares reconstruction procedure.

V.E. Circular Advection of Inflow Variation with AMR

The application of the proposed high-order CENO finite-volume scheme to the solution of circular advection at constant angular velocity is now considered in a square box. In this case the inflow function was chosen such that to test both the accuracy and robustness of the scheme as well as the capability of the high-order scheme in conjunction with AMR. The inflow variation was $u(x,0)=e^{2\,d}\,\sin^6(2\,\pi\,d)$ if $d\in[0:0.8]$, otherwise 0, where $d=x-0.4$. The boundary conditions for this problem are inflow and outflow for the bottom

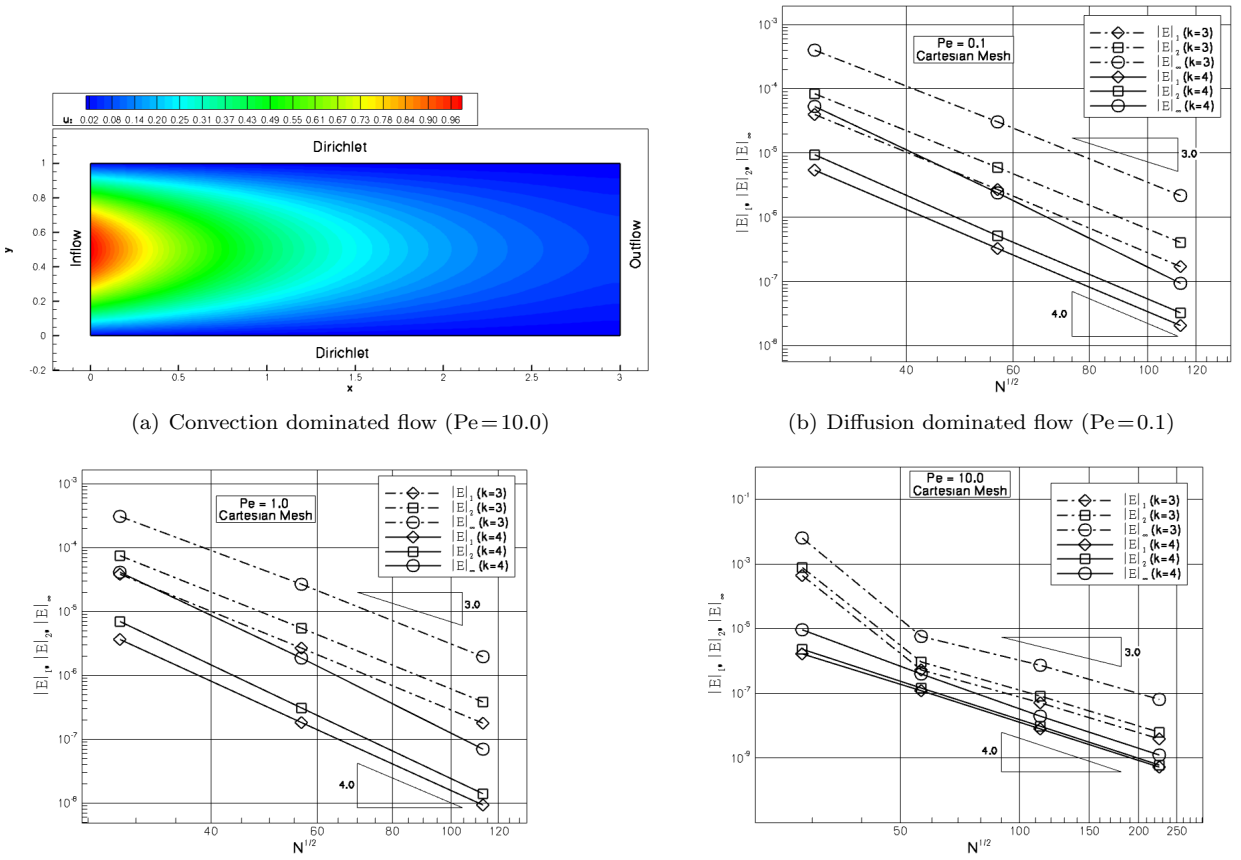

(a) Convection dominated flow (Pe = 10.0)

(b) Diffusion dominated flow (Pe = 0.1)

(c) Equal convection and diffusion (Pe = 1.0)

(d) Convection dominated flow (Pe = 10.0)

Figure 8. (a) Numerical prediction of channel flow problem on an 80×40 Cartesian mesh. (b)-(d) L_1, L_2 and L_∞ norms of the solution error as a function of mesh density obtained with cubic ($k=3$) and quartic ($k=4$) interpolants for different Péclet numbers.

and left boundaries, respectively, and far-field for the top and right boundaries. The predicted solution obtained using the 4th-order CENO scheme ($k=3$) on a final mesh consisting of 2,911 blocks and 291,100 computational cells is shown in Fig. 9(a). The solution profile along the cross-section A-A is compared against the exact solution in Fig. 9(b). The initial mesh that consists of 16 10×10 solution blocks and the final mesh are depicted in Fig. 9(c) and (e), respectively. The results clearly show that the proposed AMR scheme in conjunction with the h-refinement criteria based on the smoothness indicator of the hybrid CENO reconstruction technique is capable of refining both under-resolved (in-accurate) and non-smooth regions of the solution and will not unnecessarily refine resolved solution content. The smooth peaks are all well captured by the high-order scheme whereas the solution discontinuity is well identified by the smoothness indicator and well resolved by the hybrid CENO scheme in conjunction with the AMR procedure.

V.F. Ringleb Flow

To demonstrate the accuracy of the CENO approach for the discretization of the hyperbolic operator in the Navier-Stokes equations, numerical predictions of Ringleb's flow on body-fitted multi-block quadrilateral mesh have also been considered herein. Ringleb's flow involves isentropic, expanding, irrotational flow between two streamlines and exact solutions for this smooth continuous flow field can be determined by analytical means.[92,93] Therefore, this flow also represents a good test case to assess the influence of different sets of reconstructed variables to the accuracy of the CENO scheme. In particular, the head-to-head comparison of CENO schemes based on reconstruction of primitive and of conserved variables, respectively, has been performed herein by carrying out systematic grid convergence studies and comparing the solution accuracies in the density variable for each approach.

A transonic variant of Ringleb's flow defined by $k_{min} = 0.5$, $k_{max} = 1.2$, and $q = 0.3$ is considered here.

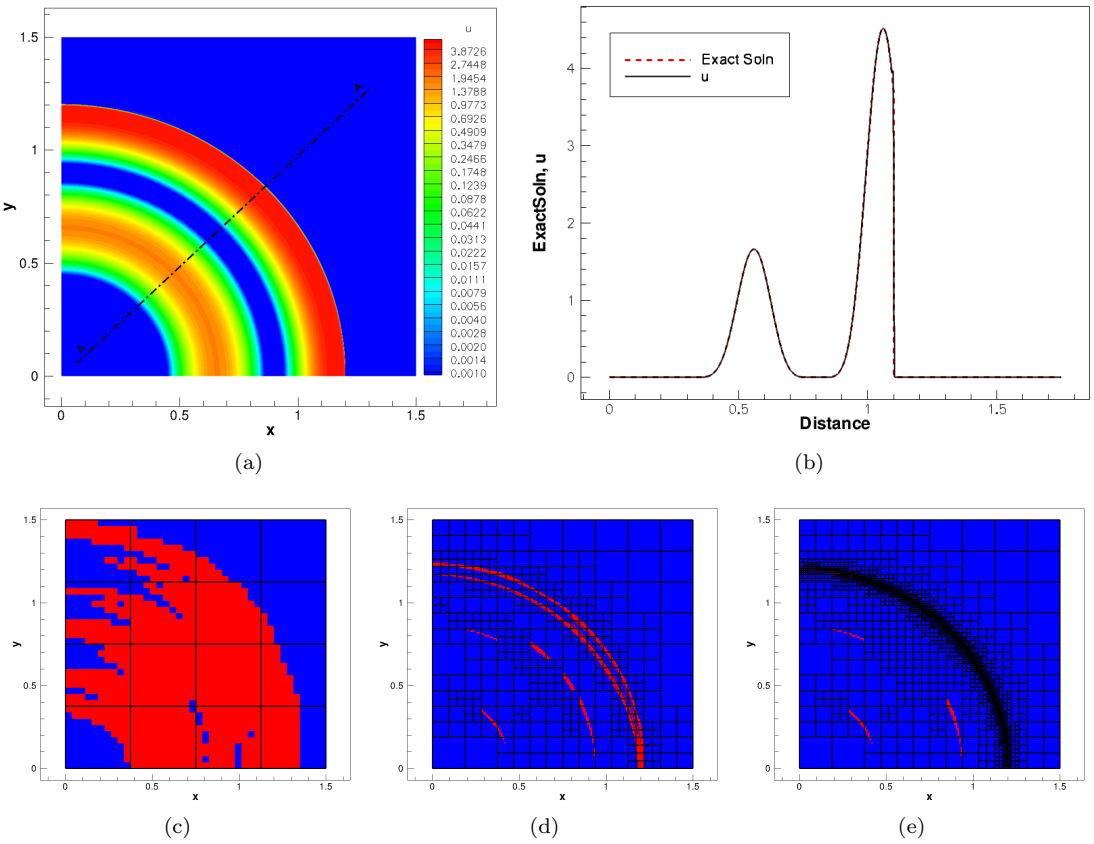

Figure 9. (a) Fourth-order ($k=3$) CENO prediction to circular advection of a smooth and discontinuous inflow variation on final mesh; (b) Comparison of numerical and exact solutions along the cross section A-A; (c) Initial mesh with 16 10×10 blocks and corresponding regions in which CENO scheme uses limited linear reconstruction (shown in red); (d) Refined mesh after 3 level of refinement (d) Final refined mesh after 6 refinement levels with 2,911 10×10 blocks and refinement efficiency of $\eta=0.955$.

For this case, reflection boundary conditions were applied along the streamline boundaries by enforcing the inviscid (slip) condition, $\vec{V}\cdot\vec{n}=0$, at all Gauss integration points via the constrained least-squares reconstruction procedure outlined in Sect. III.D.3. The predicted Mach number distribution for this flow obtained using the 4th-order CENO finite-volume scheme on a 80×80 body-fitted mesh is given in Fig. 10(a) and the L_1, L_2, and L_∞ norms of the error in predicted density and pressure obtained using the 3rd- and 4th-order versions of the CENO scheme are shown in Fig. 10(b) and (c).

For the Ringleb flow, the slopes of the L_1- and L_2-norms shown in Fig. 10(b) for the 3rd- and 4th-order CENO schemes based on reconstruction of primitive variables approach -3.06, -3.00, -3.93 and -4.02, respectively, illustrating that the accuracy of the scheme can be maintained at curved boundaries by using constrained least-squares reconstruction and accurate boundary description. The error norms of the 4th-order CENO schemes based on reconstruction of primitive (PV) and conserved variables (CV), respectively, are also compared for this supersonic flow in Fig. 10(b) and (c). The results show that the convergence rates for the two reconstruction methods based on primitive and conserved variables are again very similar and both recover the expected convergence rate in the asymptotic regime. Additionally, it is easily observed by inspecting Fig. 10(b) and (c) that the error norms in predicted solution pressure are merely a translation of those obtained in predicted solution density, thereby confirming that the same order of accuracy is recovered for all primitive solution variables. Moreover, our numerical experiments demonstrate that the error introduced by the mapping of average conserved to average primitive variables, as explained in Sect. III.D, is relatively small and does not affect noticeably the order of convergence for the scheme.

V.G. Solution of the Navier-Stokes Equations

Finally, the application of the proposed high-order CENO finite-volume algorithm to numerical simulation of flows governed by the full set of Navier-Stokes equations described in Sect. II is considered herein to illustrate

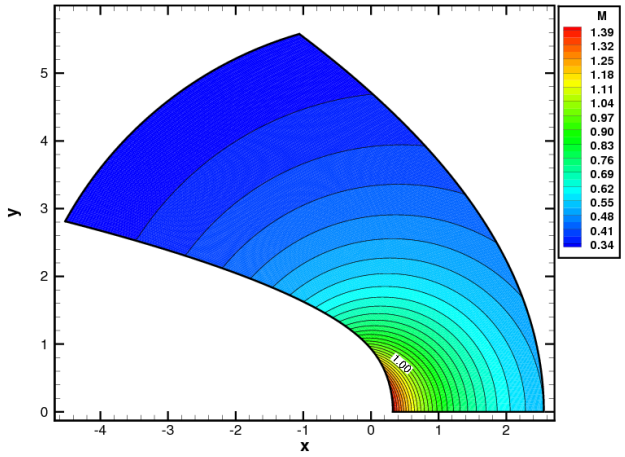

(a) 4th-order ($k=3$) CENO prediction

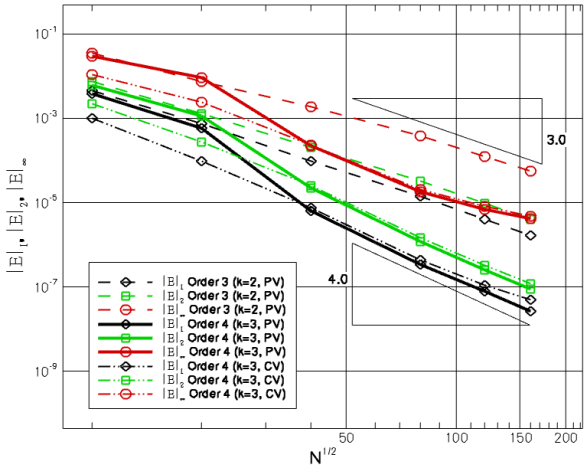

(b) Density error norms

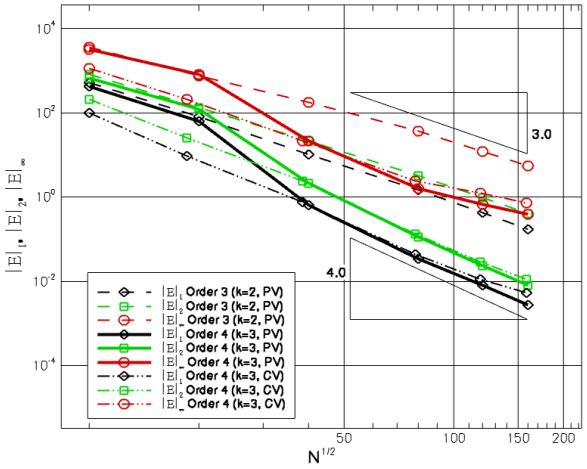

(c) Pressure error norms

Figure 10. (a) Predicted Mach number distribution for transonic Ringleb's flow obtained using 4th-order CENO scheme; and L_1, L_2, and L_∞ error norms in the predicted solution density (b) and pressure (c) for transonic Ringleb's flow obtained using the 3rd- and 4th-order CENO schemes as a function of mesh density. The error norms for the 4th-order CENO scheme are shown for both reconstruction of primitive variables (PV) and of conserved variables (CV).

the predictive capabilities of the high-order method for prediction of laminar viscous flows. Numerical simulations for fixed mesh are presented next followed by AMR results later in this section.

V.G.1. Steady Laminar Subsonic Flow Past Circular Cylinder

The predictive capabilities of the proposed CENO scheme are further examined by considering the laminar subsonic flow past a circular cylinder with a free-stream Mach number of $M_\infty = 0.1$. Numerical simulations were carried out for two Reynolds numbers, $Re = 30$ and $Re = 110$, for which no three-dimensional effects are present.[94] For $Re = 30$, the solution is a steady wake behind the cylinder as the one shown in Fig. 11(a). The unsteady flow corresponding to $Re = 110$ is solved in conjunction with AMR and discussed in Sect. V.G.2.

The geometry considered in the steady-state numerical simulations is the domain between two concentric cylinders of which the inner cylinder has a diameter $d_i = 0.0001$ and the outer cylinder has been positioned at 40 inner diameters. Five uniform but stretched towards the inner cylinder O-grid meshes were used during this study with the following resolutions: $M_1 = 3,200$, $M_2 = 12,800$, $M_3 = 51,200$, $M_4 = 204,800$ and $M_5 = 3,276,800$ computational cells. The investigation of the steady laminar subsonic flow past circular cylinder has been carried out with two numerical methods: a 4th-order (i.e. quartic reconstruction) CENO scheme and a second-order method which uses a combination of piecewise linear least-squares reconstruction and a diamond path reconstruction for the discretization of the hyperbolic and elliptic operator, respectively,

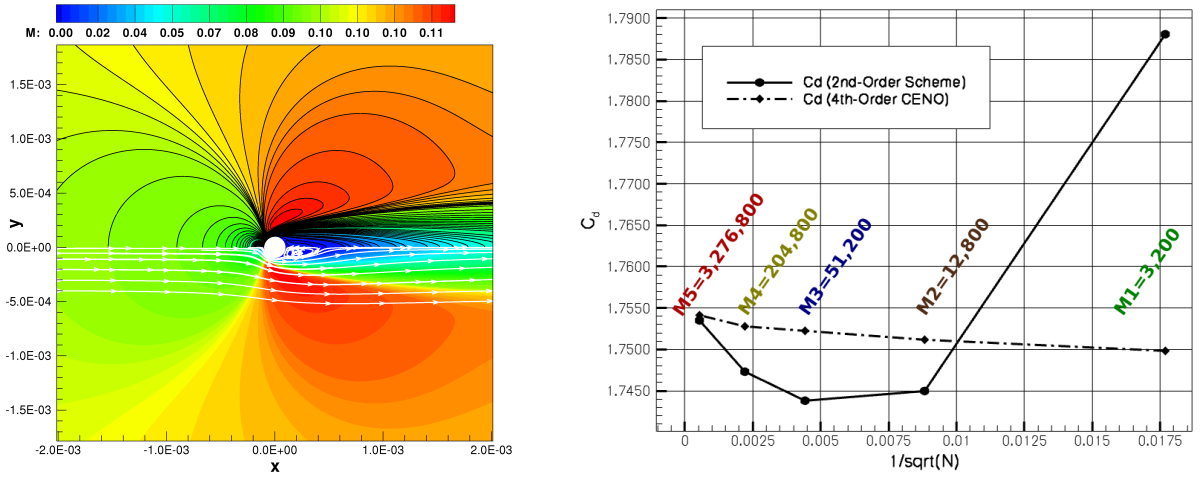

(a) Mach number prediction

(b) Predicted drag coefficients of both schemes

Figure 11. (a) Fourth-order CENO prediction of Mach number and streamlines for laminar flow over cylinder at $M_\infty = 0.1$ and $Re = 30$ on a mesh with 51,200 cells. (b) Comparison of drag coefficients predicted by the 4th-order CENO method and the 2nd-order scheme described in the text for the laminar flow over cylinder at $M_\infty = 0.1$ and $Re = 30$. The x-axis represents the equivalent mesh spacing determined as $\Delta x = \frac{1}{\sqrt{N}}$.

the details of which can be found in.[57] The imposed boundary conditions for the inner cylinder were no slip and adiabatic wall, both being enforced for the CENO scheme with the constrained reconstruction algorithm described in Sect. III.D.3. The CENO predictions of the drag coefficients were compared against those of the second-order scheme and against those calculated with the curve fits proposed by Henderson[95] which are based on an thorough numerical investigation near the onset of vortex shedding. Note that Henderson's predictions are verified against experimental data in the aforementioned paper.

The predicted Mach number distribution for laminar viscous flow around the cylinder at $Re = 30$ obtained using the 4th-order ($k = 4$) CENO finite-volume scheme on the body-fitted mesh M_3 is shown in Fig. 11(a). The drag coefficients computed based on the high-order numerical solutions for this problem were $C_D = 1.7498$ with M_1, $C_D = 1.7512$ with M_2, $C_D = 1.7522$ with M_3, $C_D = 1.7528$ with M_4, and $C_D = 1.7541$ with M_5, respectively. These values are in good agreement with Henderson's prediction of $C_D = 1.737$ and the experimental data available in the literature.[96,97]

The drag coefficients predicted by both 4th- and 2nd-order schemes are plotted in Fig. 11(b). An analysis of these results reveals several observations worth discussing. First, the predictions of both high-order and second-order methods converge to the same drag coefficient value as the mesh is refined, thus providing confidence in the validity of the two approaches. At its minimum, the difference between the predictions of the two schemes becomes only 6.5 drag counts, which is obtained on the finest mesh. Secondly, the error of the CENO predicted drag coefficient on mesh M_1 relative to the best estimation (i.e., the value obtained on mesh M_5), is only 0.245% while the mesh resolution is 1,024 times lower. In contrast, the 2nd-order method exhibits a 1.966% relative error between its drag coefficient predictions on the same meshes, which is about 8 times larger than that corresponding to the high-order CENO scheme. Furthermore, the data shows that in order to obtain the same drag coefficient error as the CENO scheme on mesh M_1 (i.e., 0.245%), the 2nd-order method requires a computational grid that is about 132 times finer than M_1.

It should be noted however, that no attempt has been made here to quantify the computational savings generated by the high-order procedure as a result of a reduced mesh resolution due to inefficiencies and inequities in the time-marching schemes which may lead to unfair comparisons between the two spatial discretizations. As the number of spatial residual evaluations required to converge to a steady-state solution greatly depends on the employed time-marching strategy, a better alternative to assess the cost of the two numerical methods is to compare the computational cost of only one spatial residual evaluation for each computational cell. Thus, time measurements on single and multiple (i.e. four) Intel Xeon CPUs, X5460@3.16GHz, with shared memory have been carried out for both high- and low-order schemes with the mesh M_3 which contains 128 blocks. The measurements indicate that the high-order CENO scheme requires about 0.0524 ± 0.0024 ms for one residual evaluation per each computational cell which is about 2.9 to 3.4 times more expensive than the cost of the second-order counterpart. These numbers imply that the

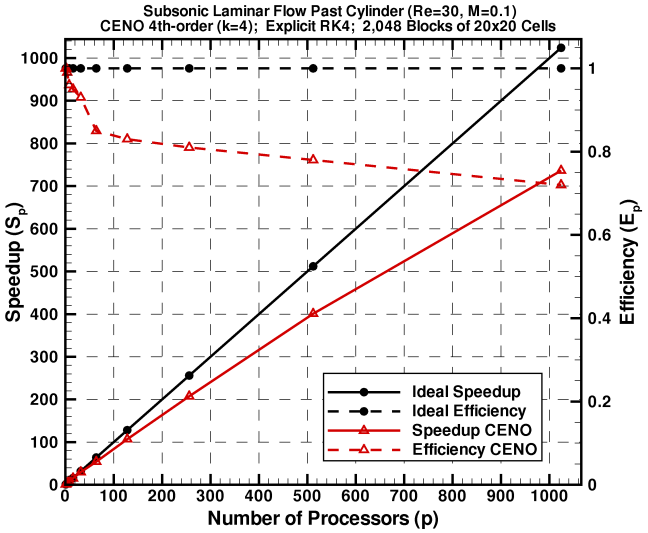

Figure 12. The parallel speedup and efficiency achieved for the steady laminar flow past cylinder by the 4th-order CENO algorithm as a function of the number of computing cores.

proposed high-order CENO scheme has the potential to provide large computational savings when accurate drag predictions are required but they will ultimately depend on how effective the time-marching strategy is in eliminating the transient component of the high-order solution.

The parallel performance of the proposed high-order CENO algorithm has also been assessed based on the steady laminar subsonic flow past circular cylinder by measuring/evaluating the parallel speedup and parallel efficiency, which are defined as $S_p = \frac{t_1}{t_p}$ and $E_p = \frac{S_p}{p}$, respectively, where t_1 and t_p are the execution times required to solve the problem by a single processor and by p processors, respectively. Herein, the parallel speedup, also known as strong scaling, has been measured by considering a fixed problem size of 2,048 20×20 blocks and a fixed number of explicit time steps, and performing the simulation on an increasing number of processors p, which had a maximum value of 1,024 in this study. Note that a perfect speedup corresponds to the ideal situation in which the execution time of the simulation on p computing cores is p times smaller than t_1. In Fig. 12 the parallel speedup and efficiency achieved by the CENO method as a function of the number of computing cores is plotted against the corresponding ideal variations of the parallel-performance parameters. The results show that the 4th-order CENO method has good parallel scalability even for computational blocks of relatively-small number (e.g., 400) of cells and manages to achieve parallel efficiencies of 0.78 and 0.72 on 512 and 1,024 computing cores, respectively. The drop incurred in parallel efficiency with increasing the processor count is an expected one as not only additional inter-block parallel communication is required as more processors are used but also the amount of computational work per computing core decreases significantly.

V.G.2. Unsteady Laminar Subsonic Flow Past Circular Cylinder with AMR

To demonstrate the predictive capabilities of the CENO scheme in conjunction with the block-based AMR algorithm for solutions of the Navier-Stokes equations governing laminar viscous flows, the unsteady vortex shedding flow over the cylinder corresponding to $\mathrm{Re} = 110$ is considered. The outer cylinder or boundary of the computational domain has been positioned in this case at 80 inner diameters d_i instead of the previously used value of 40 for the steady-state simulation in order to test the capabilities of the adaptive high-order CENO algorithm to resolve accurately flow features occurring over a wide computational domain with a reduced number of grid elements. To begin the computation, a periodic steady-state solution was obtained on an initial O-grid mesh of 32 self-similar 8×8 solution blocks with 2,048 computational cells. The corresponding drag coefficient variation with respect to physical time for this initial under-resolved solution is depicted in the lower left corner of Fig. 13. As can be seen, the mean drag coefficient is well under-predicted.

Automatic mesh adaptation directed by the proposed h-refinement criterion based on the CENO smoothness indicator of the velocity components has been further applied to this very coarse solution in the way described next to improve the representation of relevant flow features and the prediction of the drag coefficient. The initial strategy employed up to physical time $t = 0.006225$ was to incrementally improve the

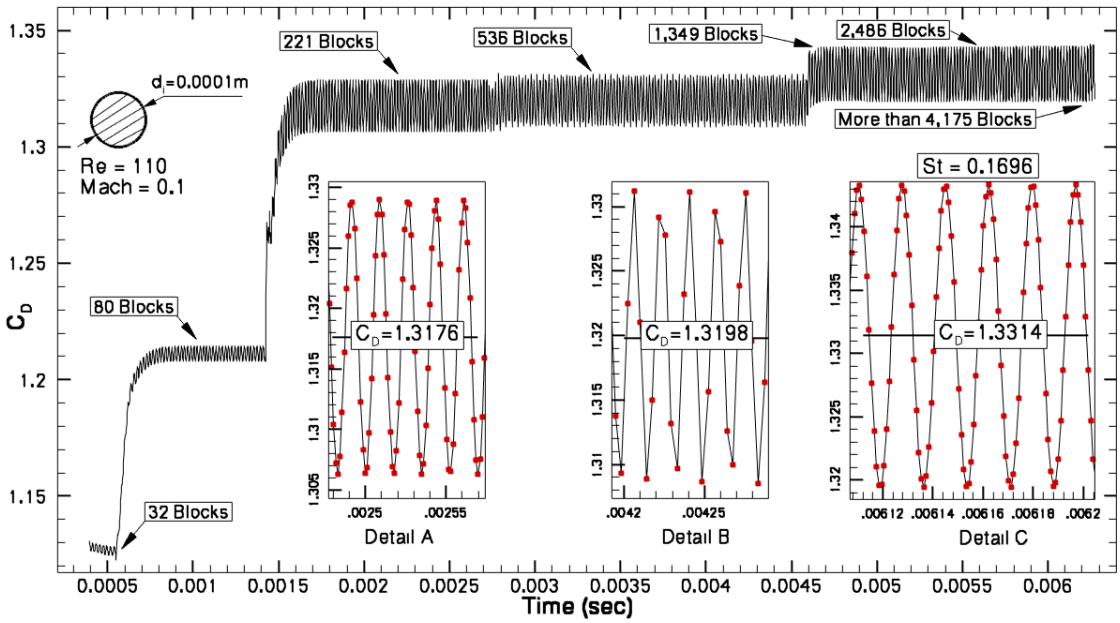

Figure 13. Variation of drag coefficient for unsteady vortex shedding flow past the cylinder as a function of physical time determined by the predicted flow field solution obtained using the 4th-order ($k=4$) CENO scheme in conjunction with the block-based AMR algorithm. The detail plates show the mean C_D value for the mesh with 221 (Detail A), 536 (Detail B) and 2,486 blocks (Detail C).

solution accuracy of the unsteady flow by generating a sequence of AMR meshes on which periodic steady-state solutions are obtained. The five meshes generated by the block-based refinement algorithm in this simulation step consists of 80, 221, 536, 1,349 and 2,486 8×8 blocks and 5,120, 14,144, 34,304, 86,336 and 159,104 cells. The drag coefficient variation following from the predicted solution on each of the five meshes is depicted in Fig. 13, which also shows the mean C_D value for the mesh with 221 (Detail A), 536 (Detail B) and 2,486 blocks (Detail C).

Following the application of the first AMR strategy, automatic mesh adaptation has been further performed for this problem dynamically at regular intervals of physical time. After an initial constant increase, the first of which being to 4,175 blocks, the AMR algorithm generated and maintained a number of blocks in the range of 10,000 to 11,000 which corresponds to 10-12 levels of refinement and mostly varied their location so as to "follow" the unsteady flow features and shed vortices. This fact can be observed in Fig. 14 in which the solution snapshots taken at physical time $t=0.006269$ is depicted to illustrate the distribution of the AMR blocks in the vicinity of the inner cylinder and the wake behind it. As can be clearly observed from the solution plot, the regions of boundary layer detachment and the vortices in the wake behind the cylinder are better resolved by the multi-block AMR grid and the mesh resolution is increased especially near and behind the inner cylinder. Notice that the domain covered by our plot span over 60 inner cylinder radii and the wake behind the cylinder gets well resolved even at large distances from the trailing edge. Notice also that the smoothness indicator recognizes the regions where interesting flow features occur such as vortices, boundary layers, flow detachment zones, and other areas characterized by sharp solution variations, and the block-based AMR algorithm adequately resolves them so as to achieve the specified level of smoothness. Nevertheless, the level of mesh resolution imposes severe restrictions on the allowable time step in the explicit time-marching scheme and consequently, a tremendous computational effort is required to simulate the many vortex shedding periods necessary to transport the convective flow features resolved near the cylinder into the far wake. Our current dynamic simulation extends over almost one period and consequently, it is anticipated that better representation of the far vortices would have been possible if more shedding periods were achieved.

The C_D curve presented in Fig. 13 exhibits convergence to a grid-independent variation as the mesh is refined by the AMR algorithm and shows that the improvements generated by the predictions on the dynamically refined meshes are minor. Our best prediction of the mean drag coefficient and Strouhal number is $C_D = 1.3314$ and $\mathrm{St} = 0.1696$, respectively, which agrees well with values from the literature. Thus, the Strouhal number based on the relationship proposed by Roshko[98] to describe the best fit to experimental data is $\mathrm{St}=0.1711$. Furthermore, the predicted mean drag coefficient compares well with the value $C_D=1.34$

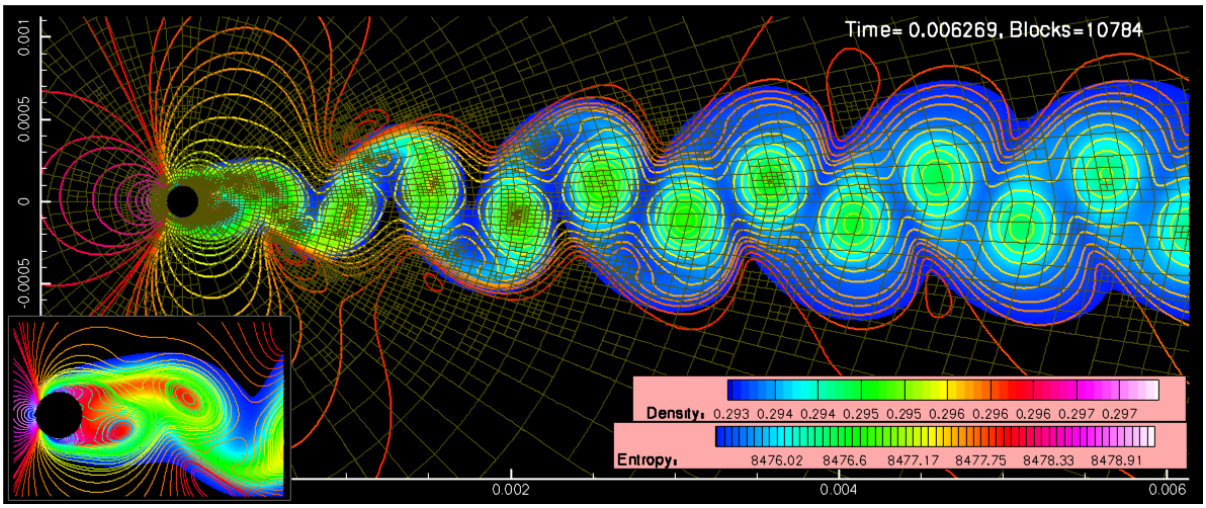

Figure 14. Predicted instantaneous density contour lines and the entropy field for vortex shedding over the cylinder on the AMR mesh with 10,787 blocks and 690,368 cells. The number of grid blocks is shown in the top right corner and the block boundaries are depicted with dark green colour. The bottom left figure is a zoom-in of the flow configuration near the interior cylinder.

reported in the computational study by Henderson.[95] Note that Sheard *et al.*[99] have also reported detailed computations of the drag for the cylinder and have compared their predictions against Henderson's and the experimentally measured drag coefficients from Wieselberger.[97] Figure 15 shows the drag coefficients obtained for both the steady (Re = 30) and unsteady (Re = 110) laminar flows past circular cylinder studied herein, plotted against the data from Sheard *et al.*[99] The plot reveals that both predictions by CENO algorithm compare very well with the previously reported values. Moreover, for Re = 110, it seems that CENO prediction is slightly more accurate with respect to Wieselberger's measurements than the curve fit value by Sheard *et al.*[99] Without overstating this result, as our study has been carried out for only one Reynolds number corresponding to unsteady flow and not for the wide range covered by the other authors, it is worth concluding that these findings provide strong support for the validity of the present implementation and indicate that the high-order CENO scheme in combination with the block-based AMR algorithm has the potential to provide reliable predictions of viscous laminar flows over complex geometries while significantly reducing the number of required computational elements.

VI. Discussion and Concluding Remarks

A new high-order CENO finite-volume scheme with AMR has been proposed for solving compressible laminar viscous flow problems on body-fitted multi-block mesh. The procedure represents an extension of the CENO approach previously developed for inviscid flow simulations to the Navier-Stokes system of PDEs governing laminar viscous flows of thermally and calorically perfect gases. The verification and validation of the proposed high-order adaptive algorithm has been accomplished by comparing predicted solutions to a variety of available analytical results, previously reported computations and experimental data. The analyzes and the results included herein confirm that the proposed numerical algorithm has many of the desirable features of a large-scale simulation framework for inviscid and viscous flows. The ability of the scheme to accurately represent solutions with smooth extrema and yet robustly handle under-resolved and/or non-smooth solution content (i.e., solutions with discontinuities) is demonstrated. The usefulness of an h-refinement criterion based on the smoothness indicator of the hybrid scheme has been evaluated and shown to provide a robust and reliable mesh adaptation algorithm that is capable of refining both under-resolved (in-accurate) and non-smooth regions of the solution and will not unnecessarily refine resolved solution content. Finally, our extensive numerical experiments indicate that this algorithm has a great potential to reduce the overall computational cost of large-scale numerical simulations thereby reducing the grid resolution required to resolved accurately solutions. Future research will involve further investigation of the CENO approach, the application of the algorithm to more complicated flows, the extension to three-dimensional problems and to hybrid structured/unstructured meshes, and the development of effective time integration techniques for the high-order CENO spatial discretization.

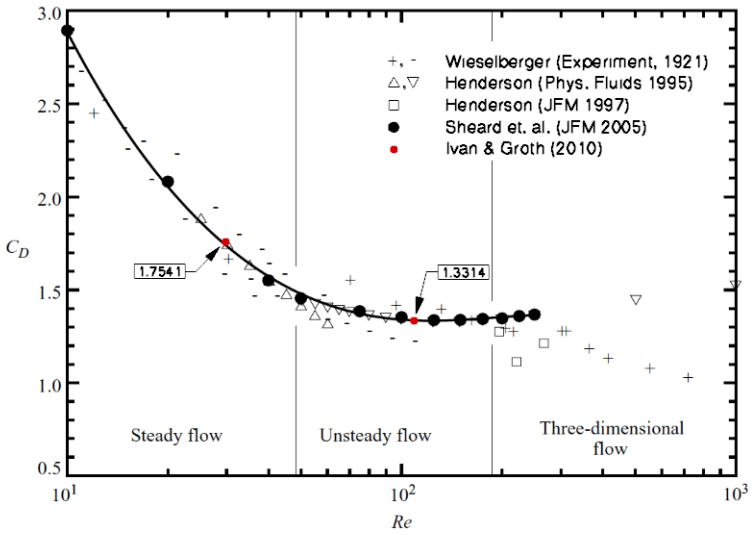

Figure 15. Depiction of the steady and mean drag coefficients predicted by the 4th-order CENO scheme for the flow past circular cylinder at $\mathrm{Re}=30$ and $\mathrm{Re}=110$ relative to previously reported values. The data obtained from Sheard *et al.*[99] includes, in addition to their computational predictions, the experimental measurements of Wieselberger (1921) and the two- and three-dimensional computations by Henderson (1995 and 1997, respectively). Additionally, the transitional Reynolds numbers from steady to unsteady flow (i.e., $\mathrm{Re}\approx 47$) and from two- to three-dimensional flow (i.e., $\mathrm{Re}\approx 189$) are indicated with vertical lines.

Acknowledgements

The first author would like to thank Prof. H. De Sterck of the Applied Mathematics Department at the University of Waterloo for offering support to this research. All computations reported herein were performed on the GPC supercomputer at the SciNet HPC Consortium. SciNet is funded by: the Canada Foundation for Innovation under the auspices of Compute Canada; the Government of Ontario; Ontario Research Fund - Research Excellence; and the University of Toronto.

References

[1]Moin, P. and Mahesh, K., "Direct numerical simulation: a tool in turbulence research," *Ann. Rev. Fluid Mech.*, Vol. 30, 1998, pp. 539–578.

[2]Jameson, L., "AMR vs. High Order Schemes," *Journal of Scientific Computing*, Vol. 18, 2003, pp. 1–24.

[3]Harten, A., Enquist, B., Osher, S., and Chakravarthy, S. R., "Uniformly High Order Accurate Essentially Non-Oscillatory Schemes, III," *J. Comput. Phys.*, Vol. 71, 1987, pp. 231–303.

[4]Abgrall, R., "On Essentially Non-Oscillatory Schemes on Unstructured Meshes: Analysis and Implementation," *J. Comput. Phys.*, Vol. 114, 1994, pp. 45–58.

[5]Sonar, T., "On the construction of essentially non-oscillatory finite volume approximations to hyperbolic conservation laws on general triangulations: polynomial recovery, accuracy and stencil selection," *Comp. Meth. Appl. Mech. Eng.*, Vol. 140, 1997, pp. 157.

[6]Jiang, G.-S. and Shu, C.-W., "Efficient Implementation of Weighted ENO Schemes," *J. Comput. Phys.*, Vol. 126, 1996, pp. 202–228.

[7]Friedrich, O., "Weighted Essentially Non-Oscillatory Schemes for the Interpolation of Mean Values on Unstructured Grids," *J. Comput. Phys.*, Vol. 144, 1998, pp. 194–212.

[8]Hu, C. and Shu, C.-W., "Weighted Essentially Non-Oscillatory Schemes on Triangular Meshes," *J. Comput. Phys.*, Vol. 150, 1999, pp. 97–127.

[9]Stanescu, D. and Habashi, W., "Essentially Nonoscillatory Euler solutions on unstructured meshes using extrapolation," *AIAA J.*, Vol. 36, 1998, pp. 1413–1416.

[10]Haselbacher, A., "A WENO Reconstruction Algorithm for Unstructed Grids Based on Explicit Stencil Construction," Paper 2005-0879, AIAA, January 2005.

[11]Wolf, W. R. and Azevedo, J., "High-Order Unstructured Essentially Nonoscillatory and Weighted Essentially Nonoscillatory Schemes for Aerodynamic Flows," *AIAAJ*, Vol. 44, No. 10, October 2006, pp. 2295–2310.

[12]Barth, T. J., "Recent Developments in High Order K-Exact Reconstruction on Unstructured Meshes," Paper 93-0668, AIAA, January 1993.

[13]Barth, T. J. and Fredrickson, P. O., "Higher Order Solution of the Euler Equations on Unstructured Grids Using Quadratic Reconstruction," Paper 90-0013, AIAA, January 1990.

[14]Ollivier-Gooch, C. F., "High-Order ENO Schemes for Unstructured Meshes Based on Least-Squares Reconstruction," Paper 97-0540, AIAA, January 1997.

[15]Ollivier-Gooch, C. F., "Quasi-ENO Schemes for Unstructured Meshes Based on Unlimited Data-Dependent Least-Squares Reconstruction," *J. Comput. Phys.*, Vol. 133, 1997, pp. 6–17.

[16]Nejat, A. and Ollivier-Gooch, C. F., "A high-order accurate unstructured finite volume Newton-Krylov algorithm for inviscid compressible flows," *J. Comput. Phys.*, Vol. 227, 2008, pp. 2582–2609.

[17]Michalak, K. and Ollivier-Gooch, C. F., "Limiters for Unstructured Higher-Order Accurate Solutions of the Euler Equations," Paper 2008-776, AIAA, January 2008.

[18]Capdeville, G., "Towards a compact high-order method for non-linear hyperbolic systems. I: The Hermite Least-Square Monotone (HLSM) reconstruction," *J. Comput. Phys.*, Vol. 228, 2009, pp. 3762–3788.

[19]Colella, P., Dorr, M. R., Hittinger, J. A. F., and Martin, D. F., "High-Order Finite-Volume Methods in Mapped Coordinates," submitted to the Journal of Computational Physics, 2010.

[20]McCorquodale, P. and Colella, P., "A high-order finite-volume method for hyperbolic conservation laws on locally-refined grids," submitted to the Communications in Applied Mathematics and Computational Science, June 2010.

[21]Colella, P. and Sekora, M. D., "A limiter for PPM that preserves accuracy at smooth extrema," *J. Comput. Phys.*, Vol. 227, 2008, pp. 7069–7076.

[22]Cockburn, B. and Shu, C.-W., "TVB Runge-Kutta Local Projection Discontinous Galerkin Finite-Element Method for Conservation Laws II: General Framework," *Math. Comp.*, Vol. 52, 1989, pp. 411.

[23]Cockburn, B., Lin, S.-Y., and Shu, C.-W., "TVB Runge-Kutta Local Projection Discontinous Galerkin Finite-Element Method for Conservation Laws III: One-Dimensional Systems," *J. Comput. Phys.*, Vol. 84, 1989, pp. 90.

[24]Cockburn, B., Hou, S., and Shu, C.-W., "TVB Runge-Kutta Local Projection Discontinous Galerkin Finite-Element Method for Conservation Laws IV: The Multidimensional Case," *J. Comput. Phys.*, Vol. 54, 1990, pp. 545.

[25]Qui, J. and Shu, C.-W., "Runge-Kutta Discontinuous Galerkin Method Using WENO Limiters," *SIAM J. Sci. Comput.*, Vol. 26, No. 3, 2005, pp. 907–929.

[26]Barter, G. E. and Darmofal, D. L., "Shock Capturing with Higher-Order, PDE-Based Artificial Viscosity," Paper 2007-3823, AIAA, June 2007.

[27]Xu, Z., Liu, Y., and Shu, C.-W., "Hierarchical reconstruction for discontinuous Galerkin methods on unstructured grids with a WENO-type linear reconstruction and partial neighboring cells," *J. Comput. Phys.*, Vol. 228, 2009, pp. 2194–2212.

[28]Kubatko, E. J., Dawson, C., and Westerink, J. J., "Time step restrictions for RungeKutta discontinuous Galerkin methods on triangular grids," *J. Comput. Phys.*, Vol. 227, 2008, pp. 9697–9710.

[29]Dumbser, M., Balsara, D. S., Toro, E. F., and Munz, C.-D., "A unified framework for the construction of one-step finite volume and discontinuous Galerkin schemes on unstructured meshes," *J. Comput. Phys.*, Vol. 227, 2008, pp. 8209–8253.

[30]Wang, Z. J., "Spectral (Finite) Volume Method for Conservation Laws on Unstructured Grids," *J. Comput. Phys.*, Vol. 178, 2002, pp. 210–251.

[31]Wang, Z. J., Zhang, L., and Liu, Y., "High-Order Spectral Volume Method for 2D Euler Equations," Paper 2003–3534, AIAA, June 2003.

[32]Liu, Y., Vinokur, M., and Wang, Z., "Discontinuous spectral difference method for conservation laws on unstructured grids," *Proceedings of the 3rd International Conference on Computational Fluid Dynamics, Toronto, Canada, July 12–16*, 2004.

[33]Huynh, H., "A flux reconstruction approach to high-order schemes including discontinuous Galerkin methods," Paper 2007-4079, AIAA, June 2007.

[34]Yang, M. and Wang, Z. J., "A Parameter-Free Generalized Moment Limiter for High-Order Methods on Unstructured Grids," Tech. Rep. 2009–605, AIAA, 2009.

[35]Yang, M. and Wang, Z. J., "A Parameter-Free Generalized Moment Limiter for High-Order Methods on Unstructured Grids," *Advan. Appl. Math. Mech.*, Vol. 1, No. 4, 2009, pp. 451–480.

[36]Wang, Z. J. and Gao, H., "A Unifying Lifting Collocation Penalty Formulation for the Euler Equations on Mixed Grids," Paper 2009–401, AIAA, 2009.

[37]Wang, Z. J. and Gao, H., "A unifying lifting collocation penalty formulation including the discontinuous Galerkin, spectral volume/difference methods for conservation laws on mixed grids," *J. Comput. Phys.*, Vol. 228, 2009, pp. 8161–8186.

[38]Abgrall, R. and Roe, P. L., "High Order Fluctuation Schemes on Triangular Mesh," *J. Comput. Phys.*, Vol. 19, No. 1–3, 2003, pp. 3–36.

[39]Abgrall, R., "Essentially non-oscillatory residual distribution schemes for hyperbolic problems," *J. Comput. Phys.*, Vol. 214, 2006, pp. 773–808.

[40]Guzik, S. and Groth, C. P. T., "Comparison of Solution Accuracy of Multidimensional Residual Distribution and Godunov-Type Finite-Volume Methods," *Int. J. Comput. Fluid Dyn.*, Vol. 22, No. 1, 2008, pp. 61–68.

[41]Abgrall, R., Larat, A., and Ricchiuto, M., "Construction of very high order residual distribution schemes for steady inviscid flow problems on hybrid unstructured meshes," *J. Comput. Phys.*, 2010.

[42]Dias, S. C. and Zingg, D. W., "A High-Order Parallel Newton-Krylov flow solver for the Euler Equations," Paper 2009-3657, AIAA, June 2009.

[43]Coirier, W. J., *An Adaptively-Refined, Cartesian, Cell-Based Scheme for the Euler and Navier-Stokes Equations*, Ph.D. thesis, University of Michigan, 1994.

[44]Delanaye, M., Aftomis, M. J., Berger, M. J., Liu, Y., and Pulliam, T. H., "Automatic Hybrid-Cartesian Grid Generation for High-Reynolds Number Flows Around Complex Geometries," Paper 99-0777, AIAA, January 1999.

[45]Sun, Y., Wang, Z. J., and Liu, Y., "Spectral (finite) volume method for conservation laws on unstructured grids VI: extension to viscous flow," *J. Comput. Phys.*, Vol. 215, No. 1, 2006, pp. 41–58.

[46]May, G. and Jameson, A., "High-Order Accurate Methods for High-Speed Flow," Paper 2005-5251, AIAA, 2005.

[47]May, G. and Jameson, A., "A Spectral Difference Method for the Euler and Navier-Stokes Equations on Unstructured Meshes," Paper 2006-304, AIAA, January 2006.

[48]Gao, H. and Wang, Z. J., "A High-Order Lifting Collocation Penalty Formulation for the Navier-Stokes Equations on 2-D Mixed Grids," Paper 2009–3784, AIAA, 2009.

[49]Haga, T., Gao, H., and Wang, Z. J., "A High-Order Unifying Discontinuous Formulation for 3D Mixed Grids," Paper 2010-540, AIAA, January 2010.

[50]Barad, M. and Colella, P., "A fourth-order accurate local refinement method for Poisson's equation," *J. Comput. Phys.*, Vol. 209, 2005, pp. 1–18.

[51]Ollivier-Gooch, C. F. and Van Altena, M., "A High-order Accurate Unstructured Mesh Finite-Volume Scheme for the Advection-Diffusion Equation," *J. Comput. Phys.*, Vol. 181, No. 2, 2002, pp. 729–752.

[52]van Leer, B., Lo, M., and van Raalte, M., "A discontinuous Galerkin method for diffusion based on recovery," Paper 2007-4083, AIAA, June 2007.

[53]van Raalte, M. and van Leer, B., "Bilinear Forms for the Recovery-Based Discontinuous Galerkin Method for Diffusion," *Commun. Comput. Phys.*, Vol. 5, No. 2–4, 2009, pp. 683–693.

[54]Oliver, T. A. and Darmofal, D. L., "An Unsteady Adaptation Algorithm for Discontinuous Galerkin Discretizations of the RANS Equations," Paper 2007-3940, AIAA, June 2007.

[55]De Rango, S. and Zingg, D., "Higher-order spatial discretization for turbulent aerodynamic computations," *AIAAJ*, Vol. 39, 2001, pp. 1296–1304.

[56]Ivan, L. and Groth, C. P. T., "High-Order Central ENO Finite-Volume Scheme with Adaptive Mesh Refinement," Paper 2007-4323, AIAA, June 2007.

[57]Sachdev, J. S., Groth, C. P. T., and Gottlieb, J. J., "A Parallel Solution-Adaptive Scheme for Predicting Multi-Phase Core Flows in Solid Propellant Rocket Motors," *Int. J. Comput. Fluid Dyn.*, Vol. 19, No. 2, 2005.

[58]Petrovsky, I. G., *Lectures on Partial Differential Equations*, Interscience, New York, 1954.

[59]Bers, L., John, F., and Schechter, M., *Partial Differential Equations*, Interscience, New York, 1966.

[60]McDonald, J. and Groth, C. P. T., "Numerical Modeling of Micron-Scale Flows Using the Gaussian Moment Closure," Paper 2005-5035, AIAA, June 2005.

[61]Northrup, S. A. and Groth, C. P. T., "Solution of Laminar Diffusion Flames Using a Parallel Adaptive Mesh Refinement Algorithm," Paper 2005-0547, AIAA, January 2005.

[62]Gao, X. and Groth, C. P. T., "A parallel adaptive mesh refinement algorithm for predicting turbulent non-premixed combusting flows," *Int. J. Comput. Fluid Dyn.*, Vol. 20, No. 5, 2006, pp. 349–357.

[63]van Leer, B., Tai, C. H., and Powell, K. G., "Design of Optimally-Smoothing Multi-Stage Schemes for the Euler Equations," Paper 89-1933-CP, AIAA, June 1989.

[64]van Leer, B., Lee, W.-T., Roe, P. L., Powell, K. G., and Tai, C.-H., "Design of optimally smoothing multistage schemes for the Euler equations," *Communications in Applied Numerical Methods*, Vol. 8, No. 10, 1992, pp. 761–769.

[65]Lomax, H., Pulliam, T., and Zingg, D., *Fundamentals of Computational Fluid Dynamics*, Springer-Verlag, New York, 2001.

[66]Hirsch, C., *Numerical Computation of Internal and External Flows, Volume 1, Fundamentals of Numerical Discretization*, John Wiley & Sons, Toronto, 1989.

[67]Hirsch, C., *Numerical Computation of Internal and External Flows, Volume 2, Computational Methods for Inviscid and Viscous Flows*, John Wiley & Sons, Toronto, 1990.

[68]Godunov, S. K., "Finite-Difference Method for Numerical Computations of Discontinuous Solutions of the Equations of Fluid Dynamics," *Mat. Sb.*, Vol. 47, 1959, pp. 271–306.

[69]Toro, E. F., *Riemann Solvers and Numerical Methods for Fluid Dynamics*, Springer-Verlag, New York, 1999.

[70]Press, W. H., Teukolsky, S. A., Vetterling, W. T., and Flannery, B. P., *Numerical Recipes. The Art of Scientific Computing 3rd-Edition*, Cambridge University Press, New York, 2007.

[71]Shi, J., Hu, C., and Shu, C., "A technique of treating negative weights in WENO schemes," *J. Comput. Phys.*, Vol. 175, 2002, pp. 108–127.

[72]Harten, A., Enquist, B., Osher, S., and Chakravarthy, S. R., Report 86-22, ICASE, April 1986.

[73]Dumbser, M. and Käser, M., "Arbitrary high order non-oscillatory finite volume schemes on unstructured meshes for linear hyperbolic systems," *J. Comput. Phys.*, Vol. 221, 2007, pp. 693–723.

[74]Capdeville, G., "A central WENO scheme for solving hyperbolic conservation laws on non-uniform meshes," *J. Comput. Phys.*, Vol. 227, 2008, pp. 2977–3014.

[75]Harten, A. and Chakravarthy, S. R., "Multi-dimensional ENO schemes for general geometries," Report 91-76, ICASE, September 1991.

[76]Harten, A., "High Resolution Schemes for Hyperbolic Conservation Laws," *J. Comput. Phys.*, Vol. 49, 1983, pp. 357–393.

[77]Ivan, L., *Development of High-Order CENO Finite-Volume Schemes with Block-Based Adaptive Mesh Refinement*, Ph.D. thesis, University of Toronto Institute for Aerospace Studies, Oct 2010.

[78]Mavriplis, D. J., "Revisiting the Least-Squares Procedure for Gradient Reconstruction on Unstructured Meshes," Paper 2003-3986, AIAA, June 2003.

[79]Lawson, C. and Hanson, R., *Solving least squares problems*, Prentice-Hall, INC, 1974.

[80]Penrose, R., "A generalized inverse for matrices," *Proceedings of the Cambridge Philosophical Society*, Vol. 51, 1955, pp. 406–413.

[81]Venkatakrishnan, V., "On the Accuracy of Limiters and Convergence to Steady State Solutions," Paper 93-0880, AIAA, January 1993.

[82]Gottlieb, J. J. and Groth, C. P. T., "Assessment of Riemann Solvers for Unsteady One-Dimensional Inviscid Flows of Perfect Gases," *J. Comput. Phys.*, Vol. 78, 1988, pp. 437–458.

[83]Roe, P. L., "Approximate Riemann Solvers, Parameter Vectors, and Difference Schemes," *J. Comput. Phys.*, Vol. 43, 1981, pp. 357–372.

[84]Einfeldt, B., "On Godunov-Type Methods for Gas Dynamics," *SIAM J. Numer. Anal.*, Vol. 25, 1988, pp. 294–318.

[85]Linde, T. J., *A Three-Dimensional Adaptive Multifluid MHD Model of the Heliosphere*, Ph.D. thesis, University of Michigan, May 1998.

[86]Linde, T., "A practical, general-purpose, two-state HLL Riemann solver for hyperbolic conservation laws," *Int. J. Numer. Meth. Fluids*, Vol. 40, 2002, pp. 391–402.

[87]Mavriplis, D. J., "Unstructured Mesh Discretizations and Solvers for Computational Aerodynamics," Paper 2007-3955, AIAA, June 2007.

[88]Gao, X. and Groth, C. P. T., "A parallel solution-adaptive method for three-dimensional turbulent non-premixed combusting flows," *J. Comput. Phys.*, Vol. 229, 2010, pp. 3250–3275.

[89]Gao, X., Northrup, S., and Groth, C. P. T., "Parallel solution-adaptive method for two-dimensional non-premixed combusting flows," in press in Progress in Computational Fluid Dynamics, July 2010.

[90]Berger, M. J. and Oliger, J., "Adaptive Mesh Refinement for Hyperbolic Partial Differential Equations," *J. Comput. Phys.*, Vol. 53, 1984, pp. 484–512.

[91]Berger, M. J. and Colella, P., "Local Adaptive Mesh Refinement for Shock Hydrodynamics," *J. Comput. Phys.*, Vol. 82, 1989, pp. 67–84.

[92]AGARD Subcommittee C, "Test Cases for Inviscid Flow Field Methods," AGARD Advisory Report 211, 1986.

[93]Coirier, W. J. and Powell, K. G., "An Accuracy Assessment of Cartesian-Mesh Approaches for the Euler Equations," *J. Comput. Phys.*, Vol. 117, 1995, pp. 121–131.

[94]Williamson, C., "Vortex Dynamics in the Cylinder Wake," *Ann. Rev. Fluid Mech.*, Vol. 28, 1996, pp. 477–539.

[95]Henderson, R. D., "Details of the drag curve near the onset of vortex shedding," *Phys. Fluids*, Vol. 7, No. 9, 1995, pp. 2102–2104.

[96]Schlichting, H. and Gersten, K., *Boundary-Layer Theory*, Springer, New York, 8th ed., 2000.

[97]Wieselsberger, C., "New data on the laws of fluid resistance," Technical Note 84, NACA, March 1922.

[98]Roshko, A., "On the Development of Turbulent Wakes from Vortex Streets," Technical Note 1191, NACA, 1954.

[99]Sheard, G. J., Hourigan, K., and Thompson, M. C., "Computational of the drag coefficients for low-Reynolds-number flow past rings," *J. Fluid Mech.*, Vol. 526, 2005, pp. 257–275.